BRNO UNIVERSITY OF TECHNOLOGY

CEITEC
Central European Institute of Technology
BRNO | CZECH REPUBLIC

TOWARDS HIGHLY-DOPED GE AND ZNO NANOWIRES: GROWTH, CHARACTERIZATION AND DOPING LEVEL ANALYSIS

VYSOCE DOPOVANÁ GE A ZNO NANOVLÁKNA: RŮST, CHARAKTERIZACE A ANALÝZA ÚROVNĚ DOPOVÁNÍ

SHORT VERSION OF DOCTORAL THESIS
TEZE DIZERTAČNÍ PRÁCE

AUTHOR
AUTOR PRÁCE
Ing. TOMÁŠ PEJCHAL
ORCID iD: 0000-0002-5093-3023

SUPERVISOR
VEDOUCÍ PRÁCE
doc. MIROSLAV KOLÍBAL, Ph.D.
ORCID iD: 0000-0002-2751-5608

BRNO 2021

Abstract

Highly-doped semiconductor nanowires represent a promising class of nanostructures with prospective applications in electronics, optoelectronics or bio-sensing. This thesis is focused on the growth and in-depth characterization of germanium and zinc oxide nanowires, with the aim of acquiring high doping levels.

The first part of the thesis deals with the growth of germanium nanowires via the vapour–liquid–solid (VLS) process. Several factors impacting the nanowire growth and morphology are described – the composition of the catalytic particle, the role of surface adsorbates and the incorporation of atoms from the catalyst into the nanowire. The nanowires are grown from gold nanoparticles either in ultra-high vacuum (the MBE-like process) or in the presence of atomic-hydrogen vapour (mimicking the CVD process), resulting in dissimilar nanowire morphology and growth direction. The combined effect of atomic hydrogen adsorption and gold catalyst spreading is revealed – being the key element explaining the difference in nanowire morphology when MBE and CVD growth techniques are utilised.

Further, the Ge nanowire growth from group-III-containing catalysts is studied, with the intention of doping the nanowires via the incorporation of atoms from the catalyst droplet. The in-situ prepared alloyed Au–Ga catalyst is found to be applicable for germanium out-of-plane nanowire growth – although the catalyst stability is lower than for pure Au. Despite a high dopant concentration in the catalyst, no gallium incorporation into the nanowire is observed. Hence, this method of nanowire doping is proved unsuitable for the material system selected.

The third part of the thesis covers the characterization of ZnO nanowires and the development of a protocol for their diffusional doping with gallium. The impact of nanowire annealing on the concentration of oxygen vacancies (V_O) is demonstrated – annealing in H_2O_2 gas decreases the V_O concentration, compared with annealing in high vacuum. Further, Ga incorporation into ZnO nanowires is documented with in-situ SEM when annealed above 350 °C. Moreover, gallium-induced decomposition of ZnO nanowires is observed above 450 °C. The concentration and spatial distribution of Ga within the nanowires is assessed using STEM EDS and a theoretical model for Ga diffusion. The correlation between the V_O concentration and the Ga incorporation into ZnO is found. Gallium concentration in the order of 10^{21} cm^{-3} is reached in the nanowires – demonstrating the suitability of the presented diffusional-doping method for achieving high Ga doping levels needed for prospective bio-sensing applications in the IR region.

Key words

Nanowire, germanium, vapor−liquid−solid growth, faceting, hydrogen, zinc oxide, doping, diffusion.

PEJCHAL, Tomáš. *Towards highly-doped Ge and ZnO nanowires: Growth, characterization and doping level analysis.* Brno, 2021. Available online: https://www.vutbr.cz/studenti/zav-prace/detail/136325. Doctoral Thesis. Brno University of Technology, CEITEC BUT. Supervisor of the doctoral thesis Miroslav Kolíbal.

Abstrakt

Vysoce dopovaná polovodičová nanovlákna představují nadějnou třídu nanostruktur pro budoucí aplikace v elektronice, optoelektronice nebo bio-senzorice. Tato práce se zaměřuje na přípravu a charakterizaci nanovláken germania a oxidu zinečnatého s cílem dosáhnout vysoké úrovně dopování.

Úvodní část dizertační práce se zabývá přípravou germaniových nanovláken metodou VLS (pára – kapalina – pevná látka). Nejprve jsou popsány faktory ovlivňující růst nanovláken a jejich morfologii – složení katalytické částice, vliv adsorbovaných atomů či molekul a potenciální inkorporace atomů katalyzátoru do objemu nanovláken. Nanovlákna připravená ze zlatých katalytických nanočástic v podmínkách ultravysokého vakua (tzv. MBE metodou) a za přítomnosti atomárního vodíku (proces napodobující podmínky CVD metod) vykazují odlišnou morfologii a směr růstu. Tyto rozdíly odhalují kombinovaný účinek adsorpce atomárního vodíku a šíření zlatého katalyzátoru na stěny nanovláken. Tento efekt je klíčový pro vysvětlení rozdílů ve výsledné morfologii nanovláken připravených MBE a CVD metodami.

Další část práce se věnuje přípravě Ge nanovláken z katalyzátorů obsahujících prvky III. skupiny a studiu jejich případné inkorporace, která by mohla vést k dopování nanovláken. Bylo zjištěno, že in-situ připravené směsné Au–Ga nanočástice lze úspěšně využít pro růst germaniových nanovláken, přestože stabilita katalyzátoru je nižší než v případě čistého zlata. I přes vysokou koncentraci gallia v katalytické částici nebyla pozorována inkorporace gallia do objemu nanovlákna. Tato metoda dopování nanovláken se tedy pro uvedenou materiálovou kombinaci ukázala jako nevhodná.

Ve třetí části práce jsou popsány výsledky charakterizace ZnO nanodrátů a vývoj metody jejich difuzního dopování galliem. Je prokázán vliv žíhání nanodrátů na koncentraci kyslíkových vakancí (V_O) – ve srovnání s žíháním v podmínkách vysokého vakua se koncentrace V_O snižuje žíháním v plynném peroxidu vodíku. Dále je zdokumentována inkorporace gallia do ZnO nanodrátů při teplotě nad 350 °C – pozorováno pomocí in-situ SEM. Při teplotě nad 450 °C dochází ke galliem indukované dekompozici ZnO nanodrátů. K určení koncentrace a prostorového rozložení Ga atomů v nanovláknech je využito teoretického difuzního modelu a STEM EDS měření nanovláken. Byla nalezena korelace mezi koncentrací kyslíkových vakancí a inkorporací gallia do objemu ZnO nanovláken. Koncentrace gallia dosahuje řádově 10^{21} cm^{-3}, což dokazuje vhodnost použité metody pro dosažení vysokých úrovní dopování, které jsou potřebné pro budoucí bio-senzorické aplikace v infračervené oblasti.

Klíčová slova

Nanovlákna, germanium, VLS růst, fazety nanokrystalů, vodík, oxid zinečnatý, dopování, difuze.

PEJCHAL, Tomáš. *Vysoce dopovaná Ge a ZnO nanovlákna: Růst, charakterizace a analýza úrovně dopování.* Brno, 2021. Dostupné také z: https://www.vutbr.cz/studenti/zav-prace/detail/136325. Dizertační práce. Vysoké učení technické v Brně, CEITEC VUT. Vedoucí práce Miroslav Kolíbal.

Table of Contents

1 Introduction

Semiconductor nanowires

Growth and characterization of semiconductor nanowires is an established field of scientific research. Nanowires represent a new class of highly attractive materials, which are intensively studied for their superior functional properties being quite different from their bulk counterparts [1]. Together with nanotubes, they exhibit a large surface-to-volume ratio, being beneficial for applications such as sensing or catalysis, where intense interaction with the environment is needed. Furthermore, thanks to their precise geometry, they represent technologically promising building blocks for future electronic and optoelectronic devices. The nanowire-based architecture allows building three-dimensional devices, significantly outperforming conventional planar technology.

In various state-of-the-art and prospective application areas, doped semiconductor nanowires represent a promising class of materials for improving the performance of present-day devices and also for designing novel architectures and devices-to-be. In modern electronics, semiconductor nanowires are already being used as conductive channels in the cutting-edge transistor fabrication, with a prospect of gate-all-around transistors. Another exciting concept is to utilize the nanowires as active sensing elements. For bio-sensing applications, doped semiconductors seem highly promising because their doping level and hence their electronic properties can be tuned and controlled, which is not possible with metals. Specifically, the plasmon resonance frequency can be tuned by the amount of activated dopants. Furthermore, multiple differently-doped segments can be built into a single nanowire, acting as separate sensing elements [2].

Doping of semiconductor nanowires

For cutting-edge and prospective applications, highly-doped semiconductor nanowires are required. The doping levels needed are predicted to be as high as 10^{20} cm^{-3} for most semiconductors (including silicon and germanium [3]). This is close to or even beyond the solubility limit of known dopants; it is difficult to achieve such levels with conventional semiconductors and doping techniques. Therefore, novel strategies and processes for effective doping are being searched for. A promising class of semiconductor materials are the transparent conductive oxides, which can be doped to high levels (up to 10^{21} cm^{-3}) by alloying with group-III metals [4]. A representative of such a material is e.g. zinc oxide (ZnO).

Currently, the doping of thin films and nanostructures is usually done by introducing a dopant-containing precursor gas into the chamber in CVD or by co-evaporation of dopant atoms in MBE during growth. According to the literature, the doping of nanowires is generally not homogeneous. There is a non-uniform doping profile – the dopant incorporation is enhanced close to the nanowire surface. This is caused by two independent effects [5]: (i) direct vapour–solid deposition of dopants onto the nanowire sidewalls [6] and (ii) preferential incorporation of dopants via VLS process close to the triple-phase boundary, where the liquid–solid interface is faceted and the supersaturation is the highest [7]. The former process can be affected by using a different gas precursor or by altering the diffusion length of dopant adatoms. For the latter one, the catalyst–nanowire interface is decisive, depending on the catalyst composition and growth kinetics. Besides the doping homogeneity, the crucial difficulty of nanowire doping is achieving high doping levels necessary for the aforementioned applications. The main obstacle is the solubility limit of dopants in conventional semiconductors (Si,

Ge, III-Vs). Furthermore, additional detrimental effects take place at high dopant concentrations; the doping efficiency decreases above a certain doping level.

For nanowires, the incorporation of dopants is no longer ruled by thermodynamics only (even if the growth and doping are performed close to thermodynamic equilibrium). Instead, it is governed mostly by kinetic effects of atom adsorption and diffusion on different facets, thus being dependent on nanowire morphology and surface termination [8]. For this reason, it proves difficult to reach the solubility limit itself, not to mention even higher dopant concentrations. On the other hand, nanowires can easily accommodate a significant amount of strain originating from impurities (including dopants) and differences in lattice constants. This lowers the number of defects, allowing the nanowires to be grown even defect-free, thus allowing higher dopant concentration to be reached.

The global objective of the thesis is the preparation and extensive characterization of germanium and zinc oxide nanowires in both undoped and highly-doped state. The aim correlates with the global scientific efforts to produce and characterize highly-doped nanowires suitable for future applications, investigating novel approaches to nanowire doping.

Detailed mechanism of vapour–liquid–solid (VLS) growth of nanowires is still not completely understood yet – regarding in particular the material transfer from the catalyst into/onto the nanowire and the impact of adsorbates passivating the sidewalls during growth onto nanowire growth and morphology. These phenomena are studied and discussed in section 2.1 for a Ge nanowire – Au catalyst material system.

Growth of germanium nanowires from dopant-containing catalysts and the possibility of incorporation of catalyst atoms into the nanowire are investigated in section 2.2. The process of catalyst incorporation could be innovatively utilized for nanowire doping. As the nanowire growth and material incorporation are non-equilibrium processes, the achievable doping level could even exceed the equilibrium dopant solubility in the nanowire [9; 10], thus outperforming current doping strategies.

Zinc oxide can be doped with aluminium or gallium to high concentration levels (up to 10^{21} cm^{-3}) [4], which could lead to plasmon-resonance-frequency shift of ZnO nanostructures up to the near-infrared region (NIR). This behaviour could be utilised e.g. for the direct detection of biomolecules. The results of development of a doping protocol and characterization procedures for ZnO nanowires diffusionally doped with gallium are presented and discussed in chapter 3.

Further, the conclusion is presented in chapter 4. The author's publications and conference contributions are summarized at the end of the thesis.

The reader may notice a dissimilar style of writing in chapters 2 and 3. The research subject of chapter 2 – Ge nanowires, their growth and characterization – has been well-established in the research group of the author's supervisor [11–13]. Therefore, the focus of this chapter is aimed at presenting the novel findings of the author in a concise form of factual and sober results. On the contrary, ZnO nanowires were a brand-new material system for our group. Their characterization was started by the thesis' author himself, building up the necessary know-how – and also instrumentation – to be utilized by other members of our research group as well. Accordingly, chapter 3 is written in a more story-telling style.

2 Germanium nanowires

The growth of Ge nanowires from gold and other catalysts under various experimental conditions is discussed in this chapter. The findings about the synergic effect of atomic hydrogen adsorption and Au catalyst spreading on the growth orientation of Ge nanowires are presented and discussed in section 2.1. Preparation of Au–Ga alloyed catalysts for Ge nanowire growth (and potential doping) and the results of the growth itself are described in section 2.2.

2.1 Revealing the synergic effect of atomic hydrogen adsorption and Au catalyst spreading on the growth orientation of Ge nanowires

Significant differences exist between Ge nanowires grown by vapour-phase techniques (CVD) and by atom evaporation from a solid source (MBE); the reasons have not been explained in a satisfactory and thorough way yet. Specifically, while the former exhibit <111> growth direction irrespectively of the substrate orientation and saw-tooth faceted morphology, the latter grow preferentially along <110> direction with smooth facets and different overall morphology. During CVD growth of Au-catalysed Ge nanowires, the nanowire sidewalls are covered with adsorbed hydrogen coming from the hydride precursors [14]; moreover, the adsorbed hydrogen (or other precursor gas fragments) significantly affect Ge nanowire morphology [15]. For MBE growth however (in experiments where atomic vapour is utilized for NW growth), the partial pressure of atomic hydrogen is quite low (i.e. $<< 10^{-3}$ Pa) – this is most probably the key element making the difference between these two growth techniques.

Within this section 2.1, the evaporation from a solid Ge source with the optional assistance of atomic hydrogen has been used. The optimal conditions for the growth of Au-catalysed Ge nanowires prepared under vacuum conditions and with the assistance of atomic hydrogen have been found. What is important, the growth direction of Ge nanowires can be changed to <111> when prepared with atomic hydrogen assistance, thus mimicking nanowire growth from hydride precursors in terms of nanowire morphology and growth direction. Furthermore, in-situ spectroscopic evidence of dissimilar gold presence on the nanowire sidewalls has been observed and its role in determining the nanowire growth direction has been demonstrated and explained.

A detailed study presenting these findings, including also in-situ growth of the nanowires in SEM and a demonstration of intentional nanowire kinking, has been published based on results presented in this thesis [16]. The study emphasizes and explains the key role of the synergic effect of atomic hydrogen adsorption and Au catalyst spreading on the growth orientation of Ge nanowires, especially during nanowire nucleation and initial stages of growth. In the following text, a concise summary of the methods and the most important results are presented.

Methods, instrumentation

Ensembles of Ge nanowires were synthesized in an ultrahigh vacuum chamber (UHV, base pressure $< 3 \cdot 10^{-7}$ Pa) coupled to a Scanning Auger Microscope system (SAM, Omicron). In order to obtain a uniform and non-conglomerate distribution of catalyst particles, Ge(111) and Ge(110) substrates were cleaned by ultrasonic treatment in acetone and isopropanol and subsequently covered with gold nanoparticles (40 nm in diameter) by dipping the sample in a 450:1 mixture of a colloidal gold solution with HCl (5%). After reaching the growth temperature in the UHV chamber, the growth was

carried out by deposition from an effusion cell (Ge flux oriented 30° to the sample surface) at a typical operation pressure of $5 \cdot 10^{-7}$ Pa in case of no hydrogen gas delivery (i.e. at ultrahigh vacuum). Note that the same set of experiments has also been performed under high vacuum conditions only (operation pressure $2 \cdot 10^{-4}$ Pa), giving identical results with respect to the studied subject. For the growth in the presence of atomic hydrogen, it was generated by cracking molecular hydrogen (introduced to the chamber by a leak valve, $p_{H2} = 2 \cdot 10^{-3}$ Pa) on a heated tungsten wire, placed in the vicinity of the sample (~ 2–3 cm).

Based on the knowledge of substrate orientation and crystal structure of the nanowire material, the information about the crystal orientation of the sidewalls and nanowire growth direction can be derived from SEM imaging. Its significant advantage is the possibility of changing the viewing angle in a wide range, thus allowing to focus on different features of the nanowire (e.g. top view, side view, alignment with different nanowire facets). Multiple examples on the use of SEM for determining the nanowire growth mode and morphology are presented hereafter.

Another technique used is Auger electron spectroscopy (AES), which can provide spatially resolved information on the chemical composition of a nanowire surface. Due to the very short mean free path of Auger electrons in the material [17], this method is extremely surface-sensitive, which makes it ideal for studying the processes on nanowire surface, such as catalyst spreading along the sidewalls. On the other hand, the extreme surface sensitivity is also the biggest disadvantage of this method due to contamination issues. In order to avoid contamination, the growth was performed in-situ in the vacuum chamber connected to the AES system; the samples were then transferred under UHV conditions for immediate measurement. The effect of contamination would become evident in the Auger spectra by (i) detecting C peak from hydrocarbons, (ii) diminishing of the peaks of desired elements and (iii) change of the overall spectrum shape.

To examine the crystal structure and chemical composition of the nanowires, ThermoFisher Titan Themis 60-300 HR-TEM was used. The nanowires were scratched off the sample onto a standardized TEM grid, localized using SEM and loaded into TEM for imaging.

Growth in (ultra-)high vacuum

The substrate temperature window for Ge nanowire growth by evaporation under high (or ultrahigh) vacuum conditions was found to be quite narrow (385 °C – 455 °C), limited from the lower end by surface diffusion of germanium atoms across the substrate and NW sidewalls, and from the upper end by their desorption [18; 19]. All the nanowires within this temperature range grow in the <110> direction, irrespective of the substrate crystallographic orientation and nanowire diameter (40 nm – 200 nm), as shown in Fig. 1a,b. The assignment of the growth direction was made by assuming the diamond cubic lattice structure and determining an angle between the growth axis and the substrate; additionally, it was verified by a detailed TEM analysis (see Fig. 4). It is interesting to note that the <110> oriented nanowires on the (110) substrate grow only perpendicular to the substrate and not in the other four possible (crystallographically equivalent) inclined <110> directions (Fig. 1b). This is different from the (111) substrate, where all three equivalent <110> growth directions are observed (see the inset in Fig. 1a). The nanowires grown under (ultra-)high vacuum have mostly a truncated rhombohedral cross section, with four major {111} and two truncating {001} sidewalls – see Fig. 2a. The latter are often overgrown and the cross section changes to rhombohedral. The growth interface is formed by two inclined (mutually tilted) {111} facets.

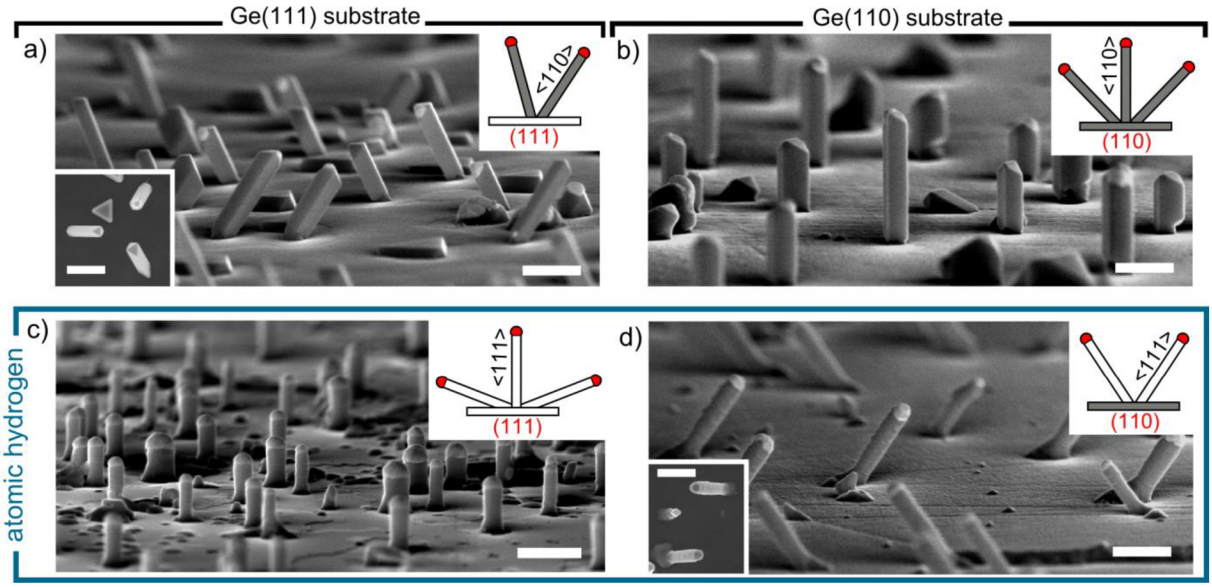

Fig. 1: SEM images of germanium nanowires grown in high vacuum (a,b) and with atomic hydrogen (c,d) on Ge(111) (a,c) and Ge(110) (b,d) substrates. The growth temperature was 425 °C in (a,b) and 385 °C in (c,d). Viewing directions are close to (a) [-110], (b) [-112], (c) [1-10] and (d) [-110] (the samples are tilted by 85° to the surface normal and by 5° to the designated viewing direction). The insets in (a) and (d) are top-view SEM images of the sample; the schematics illustrate the possible degenerate nanowire growth orientations (grey - <110>, white - <111>). Scale bars 400 nm. Published [16].

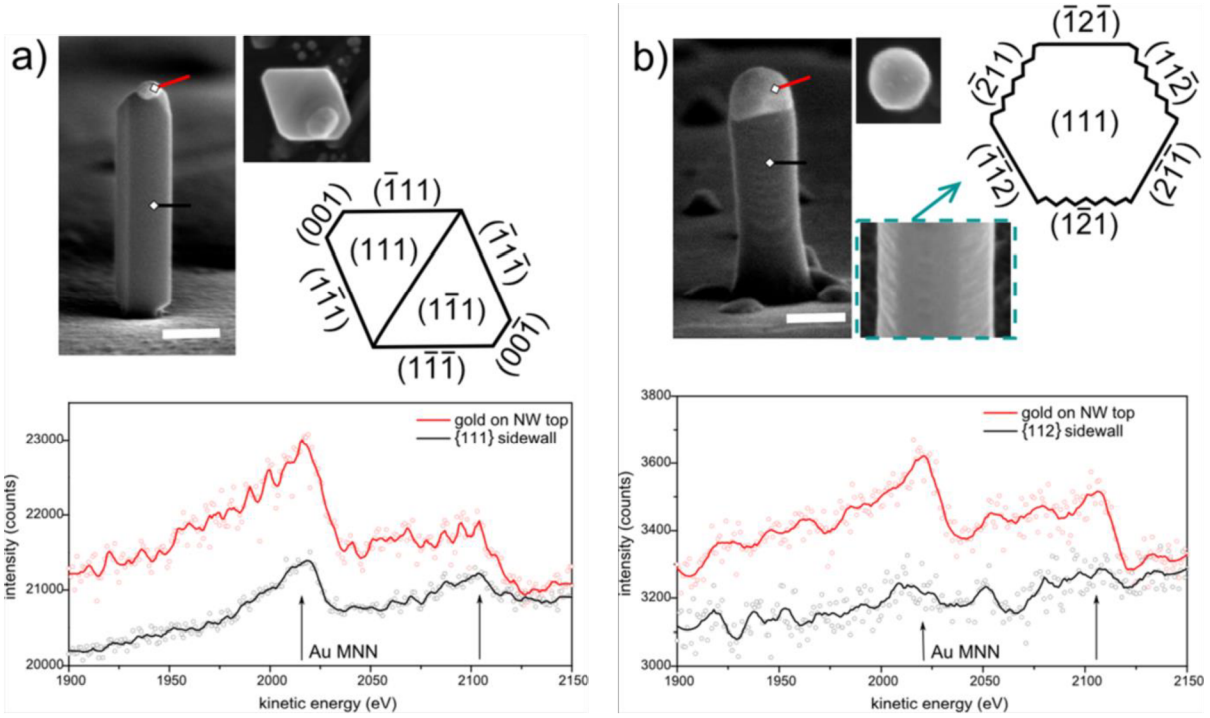

Fig. 2: Morphology of nanowires grown (a) in high vacuum on the (110) substrate and (b) with atomic hydrogen on the (111) substrate as observed ex-situ by SEM. Sketched top views show crystallographic orientations of the sidewalls and top facets; in (b) the sidewalls with pronounced sub-faceting are highlighted by zig-zag lines. A detailed view of <111> nanowire sidewalls is shown in (b), with the viewing direction marked by the green arrow. The coloured marks indicate locations where the Auger spectra were taken. The positions of the main Au MNN peaks (2015 eV and 2101 eV) are designated by the arrows. (a) Scale bar 200 nm. (b) Scale bar 100 nm. Published [16].

Growth in the presence of atomic hydrogen

The presence of atomic hydrogen in the chamber during growth changes the growth direction of nanowires to <111> (Fig. 1c,d) as well as nanowire morphology (Fig. 2b). However, this change does not apply to the whole temperature growth window. The nanowires shown in Fig. 1c,d and Fig. 2b were grown at 385 °C. At higher temperatures, increased roughening of the sidewall facets is observed; finally, at temperatures above 435 °C the <110>-oriented nanowires with clearly-defined {111} sidewalls grow despite the presence of atomic hydrogen in the chamber – see Fig. 3. This effect can be ascribed to rapid desorption of atomic hydrogen from NW sidewalls with increasing temperature, thus mimicking the high-vacuum growth. The morphology of the nanowires grown in high vacuum remains the same for a wide range of Ge deposition rate (0.075 Å·s^{-1} to 0.225 Å·s^{-1}). However, the nanowires grown at low temperature (385 °C) in the presence of atomic hydrogen adopt the morphology shown in Fig. 2b only for the lowest deposition rate (0.075 Å·s^{-1}). With increasing flux of Ge atoms (deposition rate up to 0.225 Å·s^{-1}), pronounced faceting is observed (similarly to the effect of raising temperature), while the growth direction remains <111>.

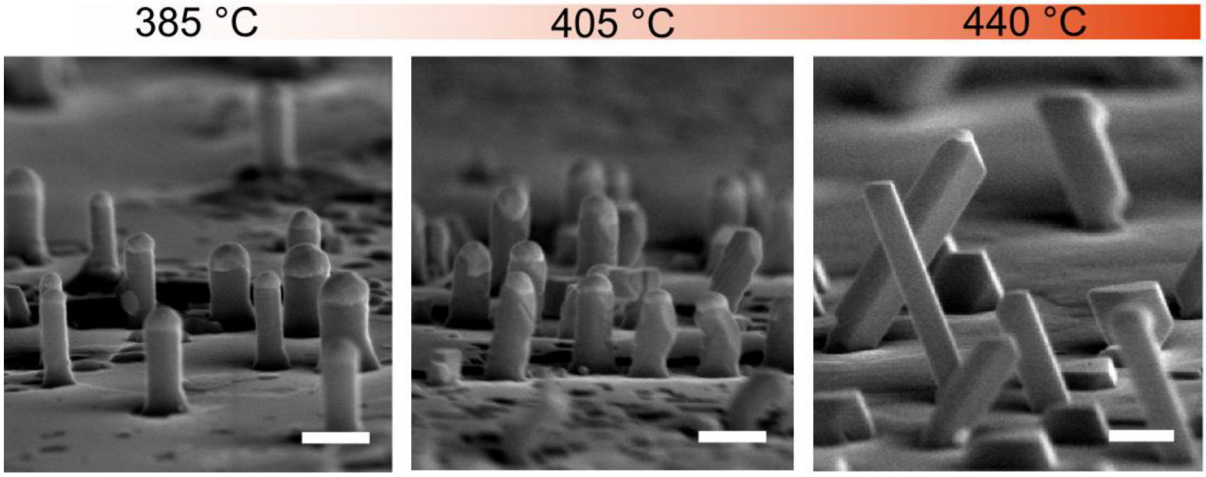

Fig. 3: Morphology and growth direction change of Ge NWs grown with atomic hydrogen at higher temperatures. The samples were grown under the same growth conditions (p_{H2} = 2·10^{-3} Pa) except the temperature, which is indicated in the figure. The nanowires grown at the lowest temperature of the available growth window exhibit relatively smooth {211} sidewalls with sub-faceting as indicated in Fig. 2b. With increasing growth temperature the faceting of nanowire sidewalls gets more significant, as {111}-oriented larger facets are often observed. Also, catalyst droplet losses become more frequent. At temperatures higher than 435 °C the nanowires change the growth direction to <110> despite the presence of atomic hydrogen in the chamber environment. Scale bars 200 nm. Published [16].

For the nanowires grown in the presence of atomic hydrogen, not all the degenerate <111> growth directions on the (111) substrate are equal, as the one perpendicular to the substrate is observed solely (Fig. 1c). In contrast to NWs grown under high vacuum conditions, all the NWs still have catalytic gold droplets on their top (visible in Fig. 1 due to different contrast). The <111> NWs grown at low temperatures with atomic hydrogen have a planar (111) growth interface (possible truncation as reported previously [20] is not visible due to droplet presence) and hexagonal cross-section (Fig. 2b). The {211}-oriented sidewalls exhibit different roughness on opposite facets (strongly resembling the sawtooth faceting of Si NWs grown by CVD) [21]. The sawtooth faceting of Ge nanowires has not been discussed in literature properly yet, although it has been already observed, especially above 300 °C [14; 15; 22; 23]. In case of gold-catalyzed Si nanowires, the partially Au-decorated sawtooth facets stabilize the growth in the <111> direction [24]. In order to confirm or exclude the presence of Au on Ge nanowire sidewalls, the nanowires were analysed by spatially-resolved Auger electron

spectroscopy. The spectra taken on the nanowire sidewalls clearly indicate the presence of a significant amount of Au on nanowires grown under the high vacuum conditions (Fig. 2a) and, in contrast, the absence of Au on sidewalls of <111>-oriented nanowires grown at low temperature with atomic hydrogen (Fig. 2b). Slight differences between the two types of {211} sidewalls of the <111> nanowires have been detected, being indicative of a trace amount of gold present on certain facets, but the signal was too weak to be conclusive.

TEM characterization of <110> and <111> Ge nanowires

According to the results presented above, the sidewalls of nanowires grown in high vacuum are covered with a thin layer of gold. Indeed, Au clusters on nanowire surface were observed using TEM imaging (not shown here). What's more, a single-crystalline nature of Ge nanowires was confirmed for both <110> and <111> nanowires (grown in high vacuum and with atomic hydrogen, respectively) – see the TEM analysis in Fig. 4. The growth direction of the nanowires and the sidewall crystallographic orientation – previously inferred from SEM analysis – were confirmed by the TEM characterization as well.

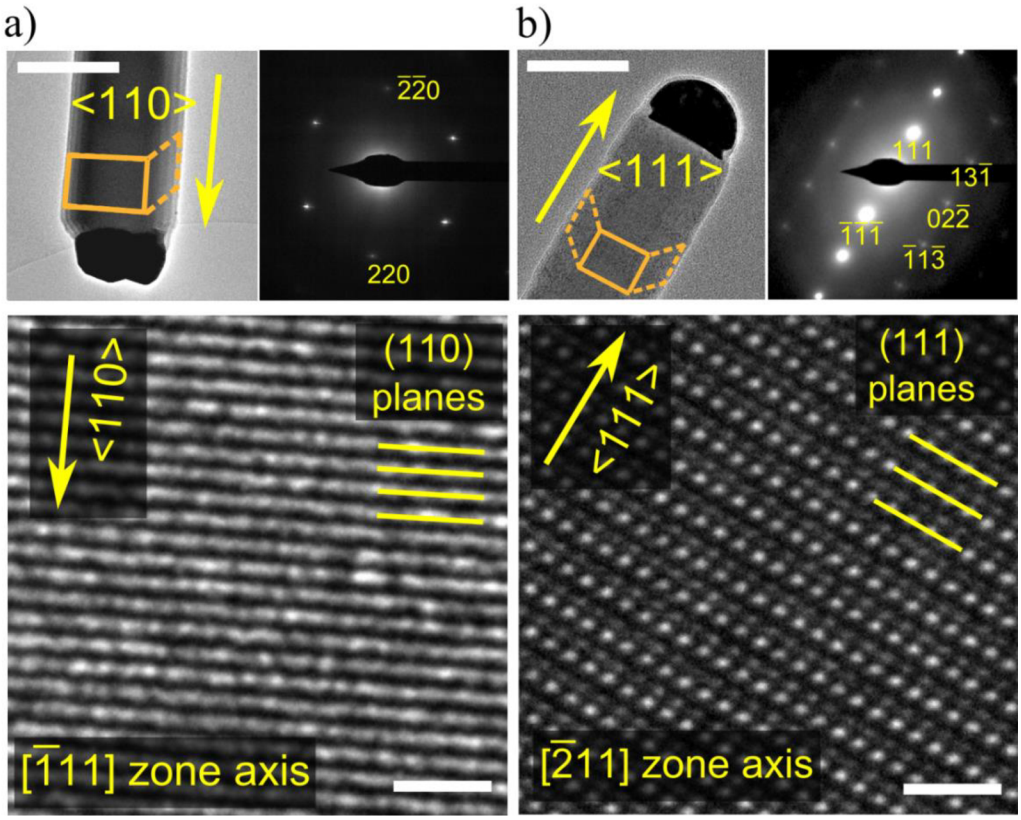

Fig. 4: TEM analysis of (a) <110> and (b) <111> nanowires grown in high vacuum and with atomic hydrogen, respectively. The lattice-plane resolved images (scale bars 1 nm) allow verifying the growth directions of both types of nanowires as determined by SEM. Additionally, selective area diffraction patterns (SAED) taken with the electron beam perpendicular to the nanowire sidewall confirm the sidewall crystallographic orientation, being {111} for <110>-oriented nanowires and {112} for <111>-oriented ones (the sidewall configuration is marked schematically in orange; the sidewall perpendicular to the electron beam is outlined with the solid line). The scale bars in overview images (always top left) are 200 nm and 100 nm in (a) and (b), respectively. TEM imaging: L. Kachtík. Published in supporting information of [16].

Discussion & Summary

The results presented so far implicate that (i) atomic hydrogen prevents gold from diffusing out of the catalyst along the sidewalls and (ii) gold promotes the formation of {111}-oriented sidewall facets. The presence of hydrogen adsorbed on germanium nanowire sidewalls up to 330 °C in case of nanowires grown from hydride precursors has been already confirmed by Sivaram et al. [14] Here, atomic hydrogen is generated more efficiently by thermal cracking of molecular hydrogen on a heated filament at high partial pressures (p_{H2} = $2 \cdot 10^{-3}$ Pa), which results in a very high adsorption rate r_{ads} (dependent on the incoming flux). The nanowire sidewalls are thus flooded with atomic hydrogen which allows to efficiently replenish adsorbed hydrogen despite the high desorption rates at enhanced temperatures used in the growth experiments. The surface diffusion of gold atoms is critically dependent on the adsorbates [25]; it has been shown by Gamalski et al. [15] that by-products of digermane decomposition passivate the surface during growth and inhibit diffusion of Au on nanowire sidewalls.

The effect of gold on germanium faceting is demonstrated in Fig. 5. As the surface energies of bare Ge facets of different crystallographic orientations are similar, the equilibrium crystal shapes are complex, exposing many different facets [26]. A stress-free homoepitaxy of Ge on Ge(111) and Ge(110) surfaces results in germanium island shapes strongly resembling those obtained using the Wulff construction (Fig. 5a,c). Experimental studies of flat Ge surfaces suggest that low-index planes are stabilized after exposure to atomic hydrogen due to (1×1)-H reconstruction [27–29]. Thus for nanowire growth at low temperatures, the sidewalls are Au-free; probably passivated with atomic hydrogen [14]. Nanowires then exhibit nearly cylindrical [30] or hexagonal cross sections as the growth is not constrained by any preferential sidewall orientation. The presence of Au on the sidewalls under conditions promoting Au diffusion (e.g. high vacuum or high temperature) dramatically changes the surface free energies in favour of {111} facets (Fig. 5b,d).

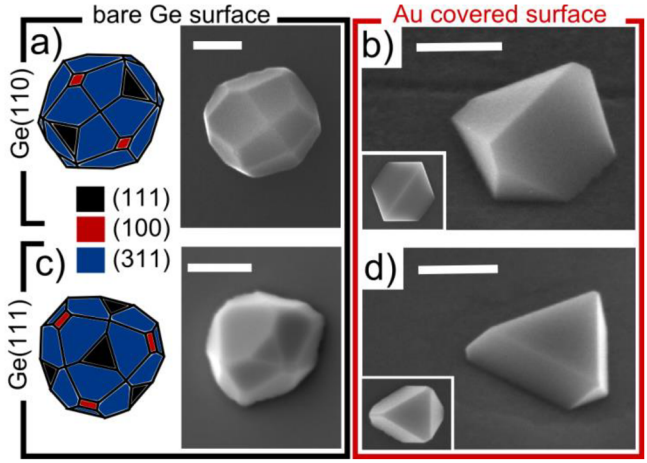

Fig. 5: Homoepitaxial growth of Ge on bare (600 °C) and gold-covered (400 °C) Ge(110) (a,b) and Ge(111) (c,d) surfaces in high vacuum. In (a) and (c) equilibrium crystal shapes are depicted (after Stekolnikov et al. [26]). The SEM images in (b,d) are tilted by 52°; (a,c) and insets in (b,d) are top views. All the scale bars are 200 nm, except in (c) (500 nm). Published [16].

To conclude, the results presented and discussed in this section show that the synergic effect of adsorbed atomic hydrogen and Au catalyst spreading is critical for determining the nanowire sidewall orientation and, consequently, the growth direction and morphology of Ge nanowires. For more details, see the published results [16].

2.2 Dopant-containing catalysts for Ge nanowire growth

The surface chemistry of the substrate and the nanowires is but one example of the wide range of parameters controlling nanowire growth in general. Another key aspect is the chemical composition of the catalyst particle itself – as it governs a plethora of physical quantities important in the nanowire growth (such as the chemical potentials, wetting angle on the nanowire material, semiconductor solubility in the catalyst, eutectic composition and temperature, diffusion and overall kinetics of the process and many others).

In contrast to gold, Ge nanowire growth from pure group-III catalysts has been reported to be difficult due to their low surface tension and the co-called Nebol'sin criterion [31]: For the VLS growth of semiconductor nanowires to be stable, only a limited range of liquid droplet's contact angles φ is thermodynamically plausible, depending on the ratio $\frac{\gamma_{SV}}{\gamma_{LV}}$, where γ_{SV} is the surface energy of the solid–vapour interface and γ_{LV} is the surface energy of the liquid droplet (see the schematics in Fig. 6a,b). For nanowire growth, the stability region is defined as follows [31]:

$$\frac{\gamma_{SV}}{\gamma_{LV}} < \frac{\sin\varphi+\cos\varphi}{\cos\delta-\sin\delta} \tag{2.1}$$

The angle δ between the conical nanowire surface and the growth axis is depicted in Fig. 6b; for constant-radius nanowires $\delta = 0$. For illustration, the inequality (2.1) is plotted in Fig. 6c for silicon nanowires growing from Au–Si liquid droplet (non-tapered nanowire, see curve 1) [31]. In regions I and III, the inequality is not met and nanowire growth is unlikely. Instead, the reverse process takes place – silicon etching and vaporization (region I and III, respectively). Region II delimits the stable growth conditions. In contrast to gold, for the low-surface-tension materials (such as Ga, Al, In, Sn) it is more difficult to satisfy the inequality (2.1) due to their lower γ_{LV}. Then, the range of energetically favourable contact angles is narrow or diminishes completely. For conical nanowires though, the range of contact angles suitable for growth is broader, see curve 2 in Fig. 6c. For this reason, short conical crystals are often observed, not followed, however, by a stable nanowire growth stage [31]. In short, stable nanowire growth occurs for the catalyst droplets of high values of surface energy γ_{LV}.

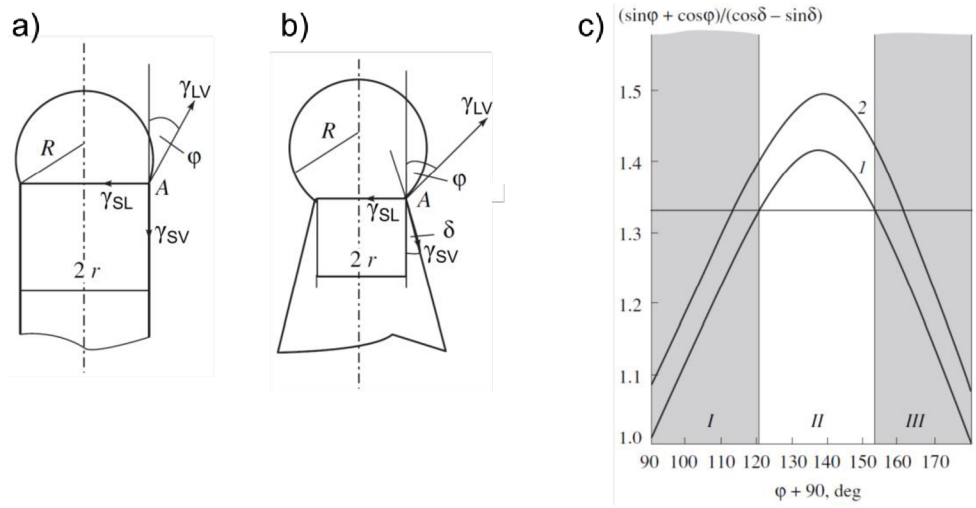

Fig. 6: Geometry of the nanowire growth: a) constant-radius nanowire (δ = 0); b) tapered nanowire (δ > 0). c) Plots of $\frac{\sin\varphi+\cos\varphi}{\cos\delta-\sin\delta}$ against the contact angle of the melt droplet atop the nanowire: (1) constant radius (δ = 0), (2) tapered nanowire (δ > 0). Shaded areas I, III are regions of whisker etching and vaporization, respectively, by the SLV mechanism; region II allows steady-state nanowire growth by the VLS mechanism. Adopted from [31].

A possible way to overcome this limitation is to modify the surface energy of the solid nanowire. Interestingly, Yu et al. [32] presented successful growth of Sn-catalysed Si nanowires, despite the low surface tension of tin. Their analysis revealed the existence of an ultrathin sidewall-spreading catalyst layer that helps to stabilize the catalyst droplet atop the nanowire during growth by modifying the effective γ_{SV} value.

Also, Si nanowire growth from Al or In–Sn catalysts and Ge nanowire growth from Sn or Ga catalysts were successfully demonstrated and what's more, massive incorporation of catalyst's atoms into the nanowires was recorded [9; 10; 33; 34]. The question of catalyst-atom incorporation into the nanowires during growth is of utmost importance. Prospective benefits are clear – the process of catalyst incorporation could be utilized for nanowire doping, even beyond the equilibrium solubility limits.

Further, other studies showed that sharp axial hetero-junctions are obtained when nanowires are grown from alloyed catalysts containing group-III element. Sharp Si–Ge interfaces were reported when grown from Au–Ga catalyst [35] or Au–Al catalyst [36] due to lower reservoir effect.

Therefore, the possibility of Ge nanowire growth from group-III-containing catalysts is studied in this section. The results of the nanowire growth are presented – concentrating on the morphology of the resulting structures and the analysis of possible dopant incorporation. Alloyed Au–Ga mixture and Au–In mixture were investigated as a catalyst for Ge nanowire growth; the latter one is detailed in the full version of the doctoral thesis.

Alloyed Au–Ga catalyst

Gallium and aluminium have very low surface tension compared to gold [32; 31; 37; 38]. Therefore, pure Ga or Al catalyst droplet is unstable on nanowire top and only in-plane growth of Ge structures is observed (see our results in the complete version of the doctoral thesis). By alloying group-III metals with other elements – such as gold, for which the stable out-of-plane NW growth has been shown above – it should be possible to stabilize the droplet and thus facilitate the out-of-plane growth. The drawback of using alloyed catalyst is in general much higher complexity in terms of material chemistry. Instead of using a simple phase diagram (mixture of supply material and the catalyst, Au–Ge for example), a tertiary phase diagram shall be considered (Au–Ga–Ge in this case). Such diagrams are more difficult to calculate or determine experimentally and they are rarely published.

Still, stable nanowire growth from alloyed Au–Ga catalyst shall be of high interest, considering possible Ga incorporation during growth, leading to nanowire doping. Two approaches will be described below: (i) Preparation of alloyed Au–Ga catalyst on a plain Ge substrate, followed by Ge deposition; (ii) formation of Ge nanowire stem grown with pure Au catalyst, followed by deposition of a small amount of gallium during the growth process, thus forming mixed Au–Ga catalyst on top of an existing nanowire. The Ge deposition and nanowire growth then continue (given that the catalyst remains stable).

The SEM micrographs of Au–Ga catalyst of various relative compositions prepared on a plain Ge wafer are shown in Fig. 7, taken ex-situ at room temperature. Gold nanoparticles from colloidal solution (40 nm diameter) were drop-casted onto Ge (111)-oriented wafer. It was then loaded into a UHV chamber, where Ga was evaporated onto the heated sample. Its deposition rate was 0.17

monolayers per minute (ML/min); sample temperature was 475 °C, being above the eutectic temperature of Au–Ga, which is 449 °C. Au–Ga alloyed droplets were formed on the surface; no pure-Ga droplets are observed under these conditions. As seen in Fig. 7, Au/Ga ratio is controlled by Ga deposition time. After cooling down for ex-situ imaging at room temperature, the alloyed mixture has separated again into Au core and Ga shell, clearly seen in the SE contrast. Different size of Au core is due to clustering of original Au nanoparticles.

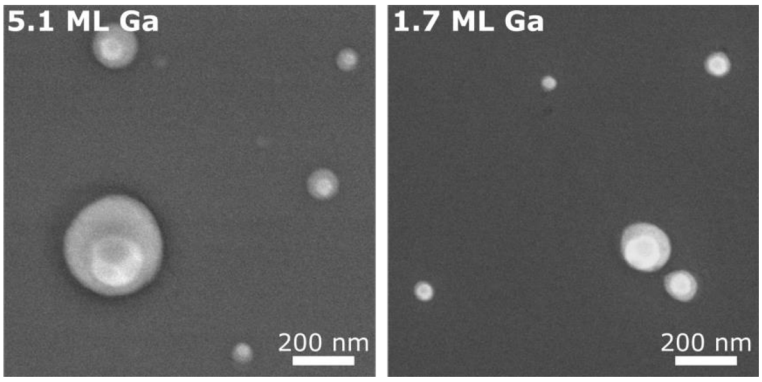

Fig. 7: SEM images of alloyed Au–Ga catalyst upon cooling down to room temperature. The images were taken ex-situ using the SE contrast. The size and composition of the catalyst particles are controlled by the amount of deposited gallium (inscribed in the images).

Keep in mind that the Au–Ga particles gradually incorporate germanium from the substrate as well, which might change the physical properties of the alloyed catalyst. (For more insight into this catalyst–substrate interaction and material uptake, being important especially during the initial stage of nanowire growth, read another paper of our research group [39].) In order to prove that the Au–Ga particles truly do alloy, a real-time in-situ SEM study was performed for such Au–Ga catalysts, see Fig. 8. Each row of images shows a different area on the sample. The sample temperature is indicated for each column. The SE contrast shows the bright Au core ringed with gallium. Indeed, the temperature series show the gradual alloying of catalyst particles.

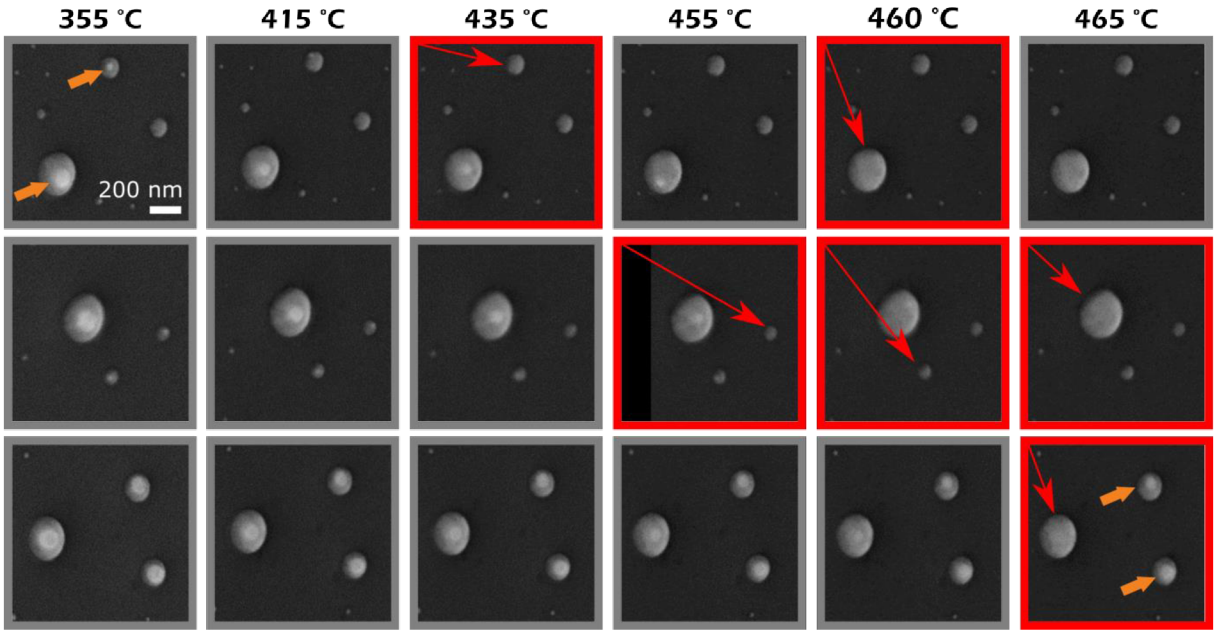

Fig. 8: Real-time in-situ SEM observation of Au–Ga alloying of catalyst particles. The annealing temperature is indicated for each column. Each row represents a different area on the sample. Red arrows indicate when the droplets become fully alloyed. Some of the droplets remain non-alloyed. The eutectic temperature of Au–Ga system is 449 °C [40].

Having demonstrated the preparation of suitable Au–Ga alloyed catalyst particles, the next step is Ge deposition onto the sample. In order to reveal the effect of catalyst composition (i.e. Ga amount in the alloyed catalyst) on nanowire growth, different amount of gallium was deposited onto the samples with Au particles prior to Ge evaporation – see the resulting morphologies in the SEM micrographs in Fig. 9. The optimal sample temperature for Ge nanowire growth from pure Au catalyst is 415 °C (Fig. 9a); it was applied to all samples shown. The amount of deposited Ge is the same as well. The only variable parameter was the amount of Ga deposited – see the value inscribed in Fig. 9b-d. The increasing amount of gallium – albeit of sub-monolayer coverage – leads to catalyst instability and formation of truncated faceted Ge pyramids instead of out-of-plane nanowires. Note that for 0.085 ML and 0.17 ML coverage (Fig. 9b,c), some nanowires are still formed, but they are shorter and much less frequent than for pure Au catalyst (see the insets).

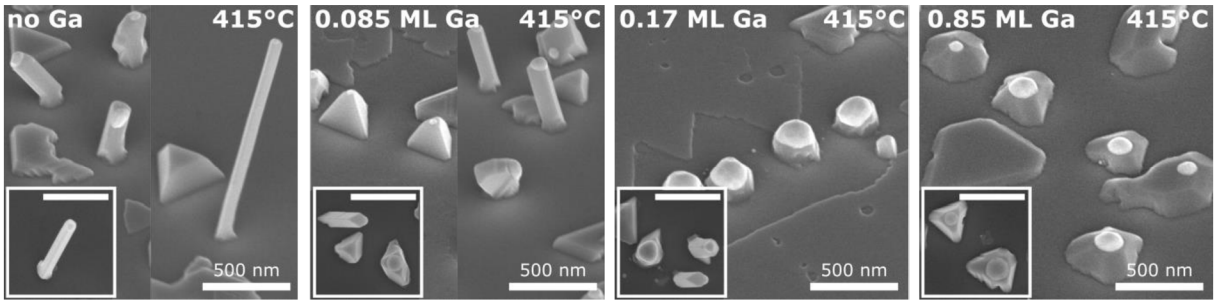

Fig. 9: Growth of Ge structures from alloyed Au–Ga catalyst of various composition. Au–Ga catalyst particles were prepared prior to Ge deposition; their composition is governed by the amount of gallium deposited (inscribed in the images). The sample temperature during Ge evaporation was 415 °C. The images were taken for sample tilted by 45°; the insets (scale bars 500 nm) show the top view.

The occurrence of Ge nanowires even for non-zero Ga coverage is a sign of possible stable growth from Au–Ga catalyst. Therefore, the effect of sample temperature during nanowire growth was studied, see Fig. 10. First, the alloyed catalyst was formed at 475 °C by deposition of 0.17 ML of gallium. After cooling down to growth temperature and its stabilization, Ge deposition was performed. Whereas the growth at 415 °C yields truncated Ge pyramids (Fig. 10a), decreasing the growth temperature to 409 °C or even 383 °C results in stable Ge nanowire growth (Fig. 10b,c). Note that the temperature of 383 °C is much lower than the optimum for the growth from pure Au catalyst (being 415 °C). In other words, even sub-monolayer Ga coverage decreases the temperature needed for Ge nanowire growth.

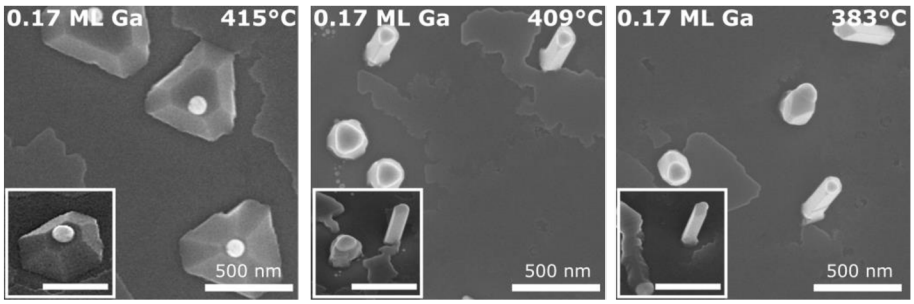

Fig. 10: Morphology of Ge structures grown from alloyed Au–Ga catalysts at various sample temperatures. Au–Ga catalyst particles were prepared prior to Ge deposition in an identical way; only the sample temperature during Ge deposition varied. The images show the top view; the insets (scale bars 500 nm) are tilted by 45°.

The catalyst stability might differ at the beginning of nanowire growth (i.e. during the formation of nanowire base) and during nanowire growth (when the droplet is pinned onto the growth facets).

The latter situation will be studied hereafter. First, a Ge nanowire stem was grown from a pure Au catalyst. Then, a small amount of gallium was co-deposited in-situ during nanowire growth, i.e. without stopping Ge evaporation. Then, only the Ge deposition continued. Therefore, the catalyst composition and surface chemistry are changed in the middle of the nanowire growth, which may or may not continue. In Fig. 11, see the results for various amount of Ga deposited in the middle of Ge deposition. The growth temperature was 415 °C for all samples. For the highest Ga coverage (0.085 ML), the catalyst becomes unstable, which results in losing the catalyst from the NW top and subsequent 3D over-growth of the nanowire with Ge material, see Fig. 11c. Interestingly, for 0.014 ML Ga coverage, some nanowires lose the catalyst as a result of its instability, whereas other nanowires change their diameter and continue growing in the original direction, see Fig. 11b. Interestingly, no kinks were observed. The diameter change observed for multiple nanowires indicates the moment when Ga was added into the catalyst. What is important, stable nanowire growth continued.

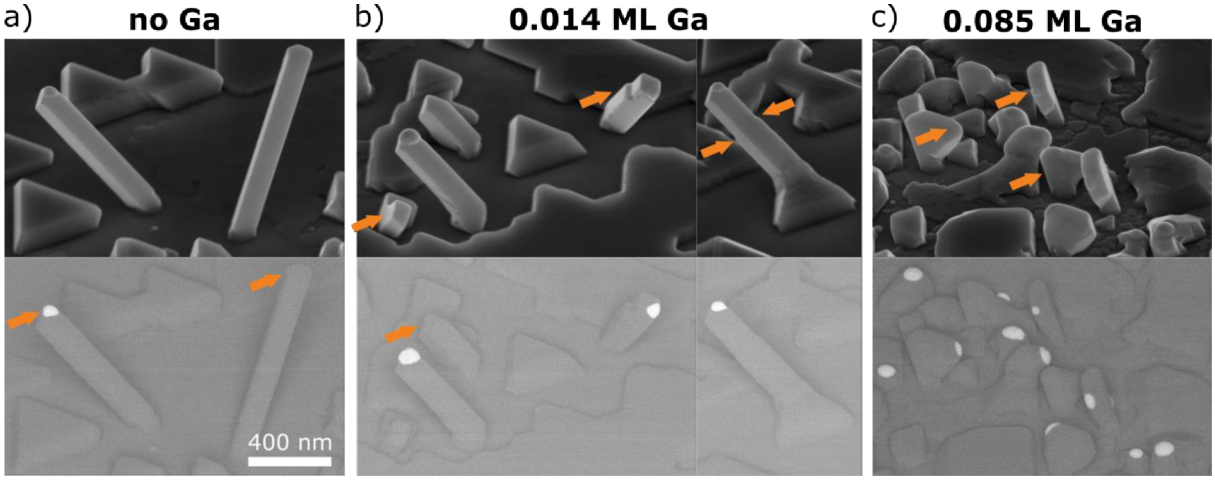

Fig. 11: Growth of Ge nanowires from Au–Ga catalyst formed during the growth. SEM images with SE contrast (top row) and BSE contrast (bottom row). The alloyed catalyst was formed by depositing gallium onto the sample with pure Au catalysts on top of previously grown Ge nanowires. The series shows the effect of deposition of different amount of gallium. The areas of interest are highlighted by orange arrows.

Further, the presence of gallium in the catalyst was confirmed by two independent methods – Auger electron spectroscopy (not shown here) and STEM EDS analysis, see Fig. 12. For this analysis, a nanowire with a slight diameter change from Fig. 11b was selected. The TEM BF and HAADF contrast images are shown in Fig. 12a,b respectively. Clearly, no crystal defects are present, despite the diameter change. Further, the EDS analysis was performed with the following results (see Fig. 12c): (i) It confirms high content of Ga in the catalyst particle (up to 4 at.%), although only 0.014 ML of Ga was deposited; (ii) the composition remains the same throughout the nanowire body, i.e. no compositional change is observed after Au–Ga catalyst formation; (iii) gallium incorporation from the catalyst into the nanowire was not proved. (The value of 0.2 at.% is below the detection limit.)

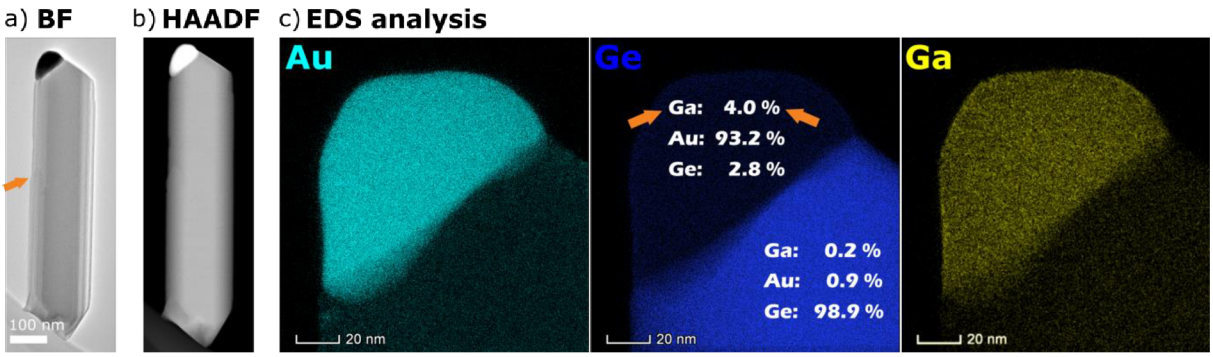

Fig. 12: a,b) TEM images (BF and HAADF contrast, respectively) of a Ge nanowire, for which an alloyed Au–Ga catalyst was formed in the middle of the growth (note the corresponding slight change in diameter, indicated by the orange arrow). A wire from the sample shown in Fig. 11b was used. c) STEM EDS analysis of this wire. The measured composition of catalyst droplet and nanowire body is inscribed. TEM imaging and EDS analysis: K. Bukvišová.

Alloyed Au–In

Next, alloyed Au–In material was studied as a catalyst for Ge nanowire growth. Similarly to Au–Ga catalyst study presented above, two distinct approaches were used:

(i) Ge nanowire stem catalysed by pure Au was grown first; then a small amount of indium was co-deposited to form alloyed Au–In catalyst on top of an existing nanowire. Then, Ge deposition and growth continued. Indium co-deposition in the middle of the growth leads to catalyst instability. The nanowire loses the catalyst from its top and no longer continues to grow. Instead, a 3D pedestal starts to grow at the nanowire base.

(ii) Preparation of alloyed Au–In catalyst on a plain Ge substrate, followed by Ge deposition. When using (111)-oriented Ge wafer, no nanowires were formed on the sample. Instead, truncated Ge pyramids were grown from the catalysts, which remained on top of these structures. Also, a 2D Ge layer is observed in between the catalysts, indicating low Ge diffusion on the wafer. Interestingly, the growth from the same Au–In catalyst performed on (110)-oriented Ge wafer leads to the formation of in-plane Ge nanowires, with the bi-metallic catalyst remaing stable.

3 Preparation of doped ZnO nanowires

Zinc oxide is a direct-bandgap semiconductor material attracting long-lasting attention both in scientific research and industry. Its wide bandgap (3.37 eV at room temperature [41]) corresponds to the UV region (wavelength of 368 nm). It belongs to a class of transparent conductive oxides. Furthermore, it can be doped with group-III metals to very high doping levels. The electron concentration of such highly-doped n-type ZnO may reach up to 10^{21} cm^{-3} [4; 41–43]. Due to its electronic properties, zinc oxide is an attractive material for applications in electronics [43], piezoelectronics [41] and optoelectronics (e.g. UV detectors) [44]. Moreover, highly-doped ZnO nanowires represent a promising material system for bio-sensing applications, as their plasmon resonance frequency may be tuned with dopant concentration down to the near-infrared region [45]. The plasmon resonance frequency in the near-IR to mid-IR region is needed to detect molecular fingerprints in the spectra.

Chapter 3 consists of several parts. The results of the AACVD method for the growth of ZnO nanowires are briefly introduced in section 3.1. Next, section 3.2 is focused on the characterization of the ZnO nanowires upon annealing in different oxidative environments. Finally, diffusional doping of the ZnO nanowires with gallium is addressed in section 3.3.

All of the measurements, imaging and data analysis presented in sections 3.2 and 3.3 were done by the author, if not stated otherwise. The exceptions are the TEM imaging and STEM EDS acquisition. However, the data analyses from these measurements were performed already by the author of the thesis himself.

3.1 ZnO nanowires grown via aerosol-assisted CVD

For the research described hereafter, ZnO nanowires prepared by a collaborating researcher Stella Vallejos (Instituto de Microelectrónica de Barcelona) are used. This section represents a short summary of the nanowires' growth method and morphology characterization, as published by Vallejos et al. (see [46; 47] for further details). The nanowires were grown via an aerosol-assisted CVD method at atmospheric pressure (AACVD). This method leads to structured growth of metal oxides without the need for catalyst seeds, i.e. via the vapour–solid (VS) mechanism; and what's more, at relatively low temperature compared to other CVD methods. Here, nanowires grown at 400 °C on a silicon wafer (using $ZnCl_2$ + ethanol solution) are employed.

Quasi-aligned nanowires of two distinct morphologies can be grown – called rods and needles in further text, see Fig. 13. Needle-like structures are grown when a higher aerosol flux is applied. Based on published XRD and TEM examination, both types are single-crystalline with preferential growth in the $[001]$ direction. As a remnant of the growth process, low chlorine contamination is present (determined with EDS; Cl:Zn = 0.05 at.%). The lattice spacing determined by HRTEM is consistent with the literature for ZnO and with the (002) plane identified by XRD. Note that in Fig. 13c,f, the crystallographic notation using the Miller indices is applied. When transformed into Miller–Bravais indices, the conversion is as follows: $\{100\}$ -> $\{10\bar{1}0\}$, $\{111\}$ -> $\{11\bar{2}1\}$, (001) -> (0001). Thus the nanowire sidewalls consist of non-polar m-plane ZnO; the top facet is a polar c-plane. The (001) top facet of rod-like nanowires is O-polar, as determined via etching experiments [48].

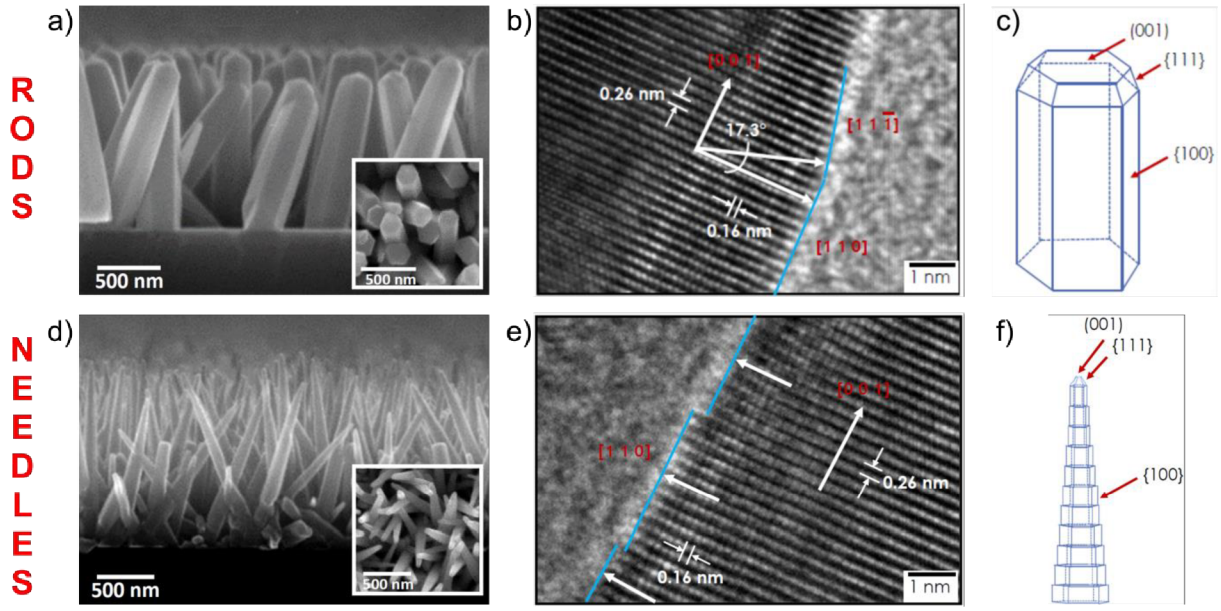

Fig. 13: ZnO whiskers grown by the AACVD method, further used for the doping study: nano-rods (a,b,c) and nano-needles (d,e,f). a,d) SEM image showing side-view of the sample. Inset: top view. b,e) HRTEM image viewed along $[\bar{1}10]$ direction. c,f) Schematics of nanowire facets orientation. Image courtesy: S. Vallejos [46].

3.2 XPS – Annealing in an oxidative environment

The presence of oxygen vacancies in ZnO can influence its properties, including dopant incorporation. Furthermore, the concentration of intrinsic defects is growth-method dependent. For both reasons, it is important to characterize the nanowires utilized within this research. In order to assess the relative concentration of oxygen vacancies in the nanowires, the XPS spectra of several samples were acquired for comparison: the as-grown ZnO nanowires and samples annealed in high vacuum and various gases at different temperatures. The upcoming doping-experiment design was taken into account (with respect to annealing temperatures and ambient gas selection). The XPS spectra of O 1s peak of these samples are presented in Fig. 14 (note that the XPS spectra have not been manipulated with respect to energy scale). Clearly, the peak is comprised of several components, being in line with the literature research [44; 49–52]; originally described and discussed for In_2O_3 material in [53]. Considering the as-grown sample (i.e. *not* annealed, black spectrum), the bulk-ZnO component (centred around 531.0 eV) and the surface-adsorbates peak (532.65 eV) are visible directly. Other samples were annealed in various ambient gases at 400 °C or 535 °C. Upon annealing, the relative intensity of the high-energy component decreased for all samples, showing that this component is indeed related to adsorbates and surface contamination of ZnO. A noteworthy feature (highlighted in the inset with a red arrow) is the "elbow" in the spectra of H_2O_2-annealed samples (red) at around 532.2 eV. Comparing it with the vacuum-annealed sample (green), the two spectra (being otherwise identical) differ significantly in this particular region (see the inset). This is indeed a sign of the intermediate component of the O 1s peak as reported in the literature – the one related to oxygen vacancies. Thus, Fig. 14 shows that annealing of ZnO nanowires in high vacuum (400 °C) and H_2O_2 gas (400 °C and 535 °C) results in different concentration of oxygen vacancies in the ZnO material. Note that the spectra of the samples annealed in H_2O_2 at 400 °C and 535 °C are identical. Based on Fig. 14, the lowest amount of oxygen vacancies was achieved by annealing in hydrogen peroxide.

This finding may play a role in the dopant-incorporation experiments presented below in section 3.3. For these experiments, the H_2O_2 oxidative agent has been chosen, given (i) the lowest V_O

concentration observed, (ii) its higher reactivity than molecular oxygen and (iii) the fact that it does not require a plasma source or a cracker to produce reactive oxygen species [54].

Regarding the morphology of the nanowires after annealing, no changes were observed in SEM up to the temperature 535 °C for any gas ambient or vacuum. At higher temperatures (600 °C and above), decomposition of the top facet and roughening of the nanowire sidewalls occur, being more pronounced for vacuum-annealed samples (not shown here).

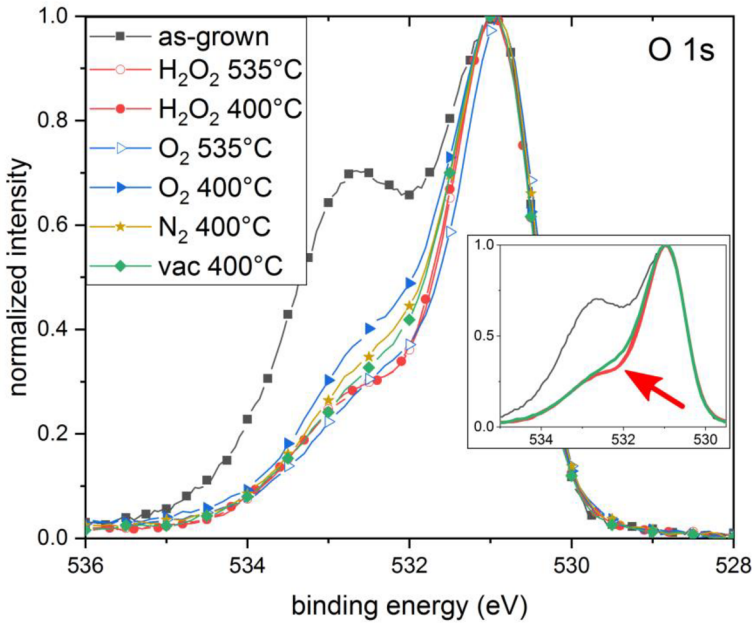

Fig. 14: Detailed XPS spectra of O 1s peak for samples after different post-growth treatment. In the inset, the spectra of the as-grown (black), vacuum-annealed (green) and H_2O_2-annealed (red) samples are highlighted for clarity.

3.3 Diffusional doping – gallium

Gallium doping of ZnO material allows to reach very high doping levels up to several at.%, thus being very promising materials for near-IR to mid-IR plasmonics. The following chapter describes the study of diffusional doping of ZnO nanowires with gallium.

The doping experiment is recorded step-by-step and the real-time in-situ SEM/AES results are presented. Further, the STEM EDS characterization of cross-sectional lamellas cut from the doped nanowires is addressed. Based on a diffusion model described, the diffusion coefficient of gallium in ZnO is derived and compared for two distinct samples of different oxygen-vacancy concentration – pre-annealed either in vacuum or in H_2O_2 environment.

Real-time in-situ SEM/AES

In further text, two distinct samples from the same growth-batch will be inspected and compared. The two samples differ in the pre-annealing environment (vacuum or H_2O_2 gas) so that the relation between oxygen-vacancy concentration and Ga incorporation can be assessed. The samples are labelled "V_O-rich" for the sample with a large concentration of O vacancies (caused by pre-annealing in vacuum; see the reasoning and XPS results in chapter 3.2) and "V_O-poor" for the sample with a low concentration of O vacancies (caused by pre-annealing in H_2O_2 gas).

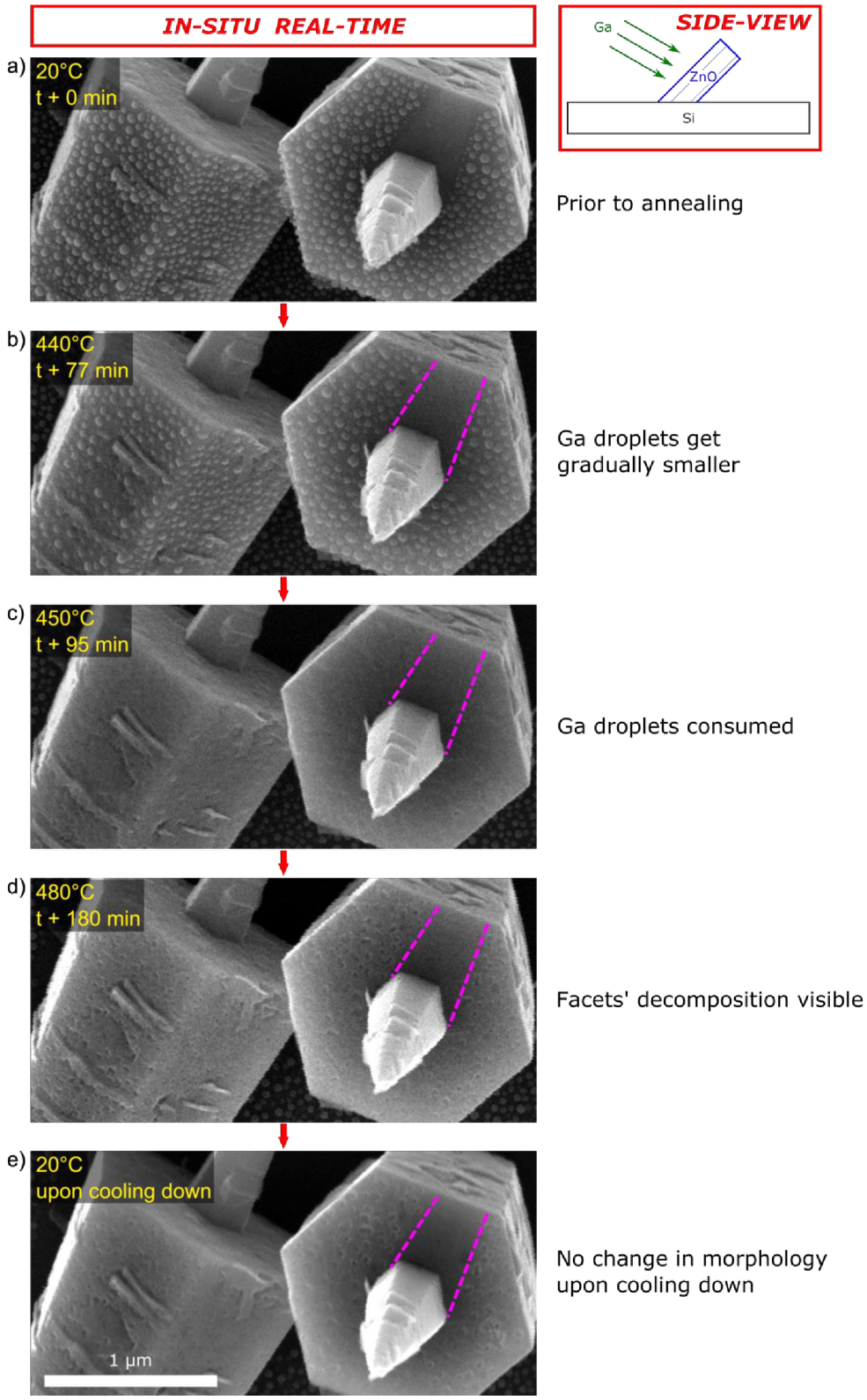

Fig. 15: Flowchart of gallium–incorporation experiment: Real-time in-situ SEM study of Ga incorporation into ZnO wires at elevated temperatures and Ga-induced ZnO decomposition. The timestamp (since the start of annealing) and sample temperature are indicated in each micrograph. After Ga deposition at room temperature (a), the sample is heated up step by step. Ga droplets get gradually smaller (b) until they get completely consumed (c). After that, the wire facets start to decompose (d) – both the sidewalls and the top facet of the wire (despite being crystallographically different). Note that the decomposition takes place only on areas originally decorated with gallium – see the difference for the shadowed area on the top facet, marked by the purple dashed lines. e) Final sample morphology after the annealing sequence and cooling down to room temperature. No gallium precipitation is observed. Note that gallium has not desorbed, but rather incorporated into ZnO (as proved by AES and EDS, see further text).

The experiments were performed in an apparatus that provides low residual pressure (UHV conditions, base pressure down to 10^{-9} Pa) and the possibility of in-situ SEM/AES characterization during sample annealing. The aim is to inspect the process of diffusional doping in-situ in real time, using combined SEM and AES techniques.

For the in-situ SEM/AES experiment, the V_O-rich sample is used. Its preparation was following: It was pre-annealed in vacuum (300 °C, $4 \cdot 10^{-6}$ Pa) for 30 minutes. After cooling down to room temperature, 9 nm of Ga was deposited onto the sample (Ga flux direction was 30° to the sample surface; chamber pressure $4 \cdot 10^{-6}$ Pa). Then the sample was transferred in-situ to the AES chamber with a base pressure of $7 \cdot 10^{-9}$ Pa. As the gallium flux is oriented 30° to the sample surface, only one side of the nanowire is decorated with gallium. This gives us the possibility to study both Ga-decorated and bare-ZnO facets at the same time under the same conditions.

The gallium–doping experiment flowchart is presented in Fig. 15. Two adjacent nanowires decorated with gallium were selected to undergo the in-situ annealing with real-time SEM imaging. Note that due to shadowing of the incident Ga flux, there are both Ga-decorated and non-deposited areas on the top facet of the right-hand-side wire (well seen in Fig. 15a). The sample was annealed gradually so that the dynamics of morphological changes could be observed in real time; the sample temperature and time-stamp since the beginning of annealing is inscribed in the SEM micrographs. The maximum chamber pressure during annealing was $2 \cdot 10^{-7}$ Pa. After annealing the sample up to 480 °C, the wires were inspected with the AES technique (still at 480 °C; results discussed below) and cooled down to RT (Fig. 15e). The SEM micrographs were acquired using a 10 keV beam with a probe current 100 pA. No effects of electron beam irradiation were observed.

Let's have a look at the interaction of Ga with the ZnO wires step by step. In Fig. 15a, two ZnO wires upon Ga deposition are imaged at room temperature (prior to the beginning of annealing, t = 0 min). Ga droplets have covered the sidewalls of the left wire and part of the top facet of the right wire – the shadowed area without gallium deposit is clearly seen. Note the sharp borders indicating low Ga surface diffusion at room temperature (indicated by dashed lines in the other micrographs). Next, the sample was heated up to 440 °C (Fig. 15b, t + 77 min). Gallium droplets get gradually smaller, i.e. no Ostwald ripening is seen. Therefore, either Ga desorption or its diffusion into ZnO volume takes place. Also, no damage to the ZnO wire is observed. (Note that the decrease in Ga droplets volume was evident already at 350 °C, t + 48 min; not shown here.) Having increased the temperature to 450 °C (Fig. 15c, t + 95 min), Ga droplets have completely disappeared and smooth ZnO facets are seen. Interestingly, as will be shown later by AES (Fig. 16), gallium undoubtedly remains present on such facets. Therefore, Ga does *not* desorb from ZnO, but rather incorporates into the nanowire. After further temperature increase and time delay (Fig. 15d, 480 °C, t + 180 min), the surface of the wire starts to be decomposed (see the etched-away pits). Notably, this decomposition occurs only on areas of previous Ga deposition – mind the shadowed top-facet area, which remains smooth and intact (marked by the dashed purple lines). Therefore, the observed ZnO decomposition is *not* a temperature effect itself; the ZnO etching is gallium–induced. (This is in agreement with previous results, where vacuum–annealing of as-grown ZnO nanowires up to 535 °C did *not* induce their thermal decomposition.) Figure Fig. 15d shows the sample conditions when the AES measurements presented in Fig. 16 were performed. After that, the sample was cooled down to room temperature (Fig. 15e). The sample preserved the same morphology as at the end of the annealing series (480 °C), including the distinction between the etched and the intact area. Note that *no* gallium droplets have

formed on the wire after cooling down – indicating permanent change and real incorporation (as opposed to forming a thin surface layer). Also, *no* gallium–oxide remnants have formed under these conditions.

The AES spectra taken at elevated temperature from both the partially-decomposed (etched) and the intact (shadowed) area of the top facet of the ZnO wire shown in Fig. 15d are presented in Fig. 16a (C and O peaks) and Fig. 16b (Ga and Zn peaks).

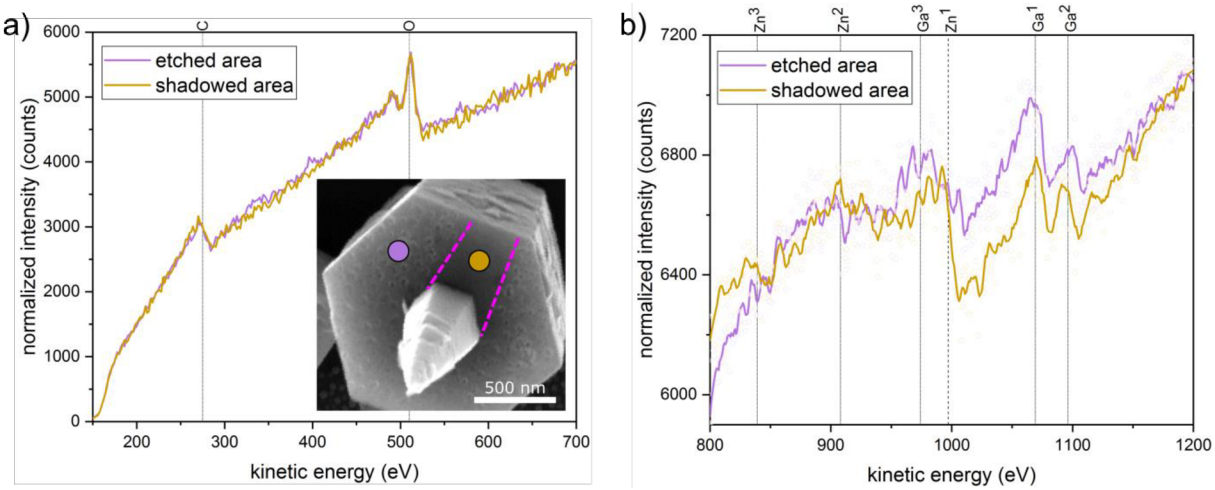

Fig. 16: Normalized AES spectra taken on different areas of the top facet of ZnO wire shown in Fig. 15d. Here, see the inset, where the location of spectra acquisition is illustrated (purple spot for the etched area, golden for the shadowed area). The spectra were acquired at 480 °C, i.e. at the end of the annealing procedure. a) Carbon and oxygen peaks are identical for both areas inspected. b) Gallium peaks were identified on both spots, including the area originally shadowed from gallium deposition. This indicates Ga surface diffusion into such areas during annealing. The zinc signal is high in the shadowed area and weak in the etched area (over-deposited with Ga in the beginning).

Two points are worth noting here:

- In the AES spectral region between 800 eV and 1200 eV, there shall be three zinc peaks and three gallium peaks. The upper indices in Fig. 16b indicate how intense the peaks shall be (e.g. Ga^1 being the highest and Ga^3 the least pronounced). Note that this labelling is applied for the purpose of this thesis only to ease the evaluation and description.
- Given the rougher (i.e. "more 3D") morphology of the etched area, spectra normalization was applied. Here, normalization means the multiplication of measured spectra so that they reach the same background intensity at the upper end of the energy range.

Carbon peak is visible in both spectra due to contamination. More interestingly, gallium is also visible in both spectra. This is not surprising in the area of previous Ga deposition (and incorporation), yet gallium present in the "shadowed" area indicates higher Ga surface diffusion at elevated annealing temperatures than expected from the sharp boundary between the etched and intact parts of the top facet. Still, the Zn^1 peak is more visible in the shadowed area, see Fig. 16b. (Gallium presence after annealing on the facets not originally decorated with gallium is further confirmed by STEM EDS measurements, see further text and figures in this chapter. Lower Zn^1 peak on the etched area – where Ga was deposited – corresponds with EDS results as well; smaller Zn concentration was observed where Ga had been deposited, see e.g. Fig. 18.)

Cross-sectional STEM EDS & Diffusion model

The key question is whether gallium diffuses into the ZnO nanowires and if so, what is the diffusion kinetics like. This chapter presents STEM EDS characterization of the two distinct samples introduced above (i.e. V_O-rich and V_O-poor, differing in the pre-annealing environment) that underwent the gallium-treatment procedure. Cross-sectional lamellas cut from the nanowires are inspected. Out of the V_O-rich sample, two nanowires are characterized – the one utilized for the real-time SEM/AES characterization presented above and another one, not influenced by such examination. Subsequently, a nanowire from the V_O-poor sample is characterized. Further, a simple diffusion model is introduced, out of which the diffusion coefficients and diffusion lengths of gallium in such ZnO nanowires are extracted. At the end of the section, these quantities are compared for both samples.

In order to characterize the spatial distribution of gallium within the V_O-rich ZnO nanowires after the annealing process described above, a cross-sectional STEM EDS analysis was performed – see the SEM micrographs of two selected nanowires in Fig. 17. The wire indicated in Fig. 17a is the same as observed during the annealing process in SEM/AES (i.e. the left wire in Fig. 15). This wire will be referred to as Wire-2 in further text. The other wire to undergo the EDS analysis (shown in Fig. 17b, referred to as Wire-1) has not been imaged or characterized before. This ensures that the wire has not been influenced by SEM or AES measurements. This might prove important, as the AES technique could lead to local heating of the sample – note the high current and electron energy used (1 nA, 10 keV). The location of the TEM lamellas cut from the wires is indicated by dashed red lines in Fig. 17. The aim is to inspect the cross-section of the wires and measure the EDS profiles of gallium. The samples were cut with a xenon-plasma focused ion beam (ThermoFisher Helios 5 PFIB DualBeam). (Note that a standard Ga FIB cannot be used as it would compromise the EDS measurement by possible gallium implantation.) The lamellas were cut perpendicularly to the substrate surface; therefore, they are *not* perpendicular to nanowire axes. This will be taken into account for the correct interpretation of gallium depth-profiles measured by EDS.

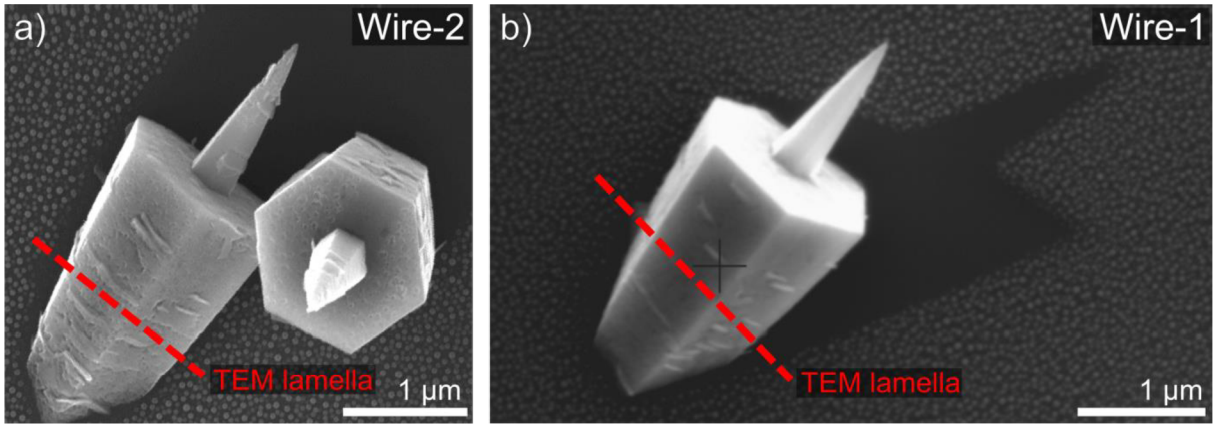

Fig. 17: ZnO wires from V_O-rich sample after Ga-incorporation procedure – location of the TEM lamellas for EDS characterization (indicated by red dashed lines).

The amount of deposited gallium is different for each facet on the wire due to its unique geometric orientation relative to the incoming Ga flux. Therefore, there are basically three-in-one independent experiments on the wire – one for every facet exposed. Based on the distances and angles measured in the top-view SEM image of the wire (showing a clear shadowing effect of the incoming gallium

flux, see e.g. Fig. 17b), it is possible to calculate the unit vector of Ga flux $\overrightarrow{Ga_j}$ and the unit vector $\overrightarrow{k_j}$ normal to a selected sidewall. Then, gallium dose for a particular facet (relative to a maximum Ga dose for a facet perpendicular to Ga flux) can be estimated based on the experiment geometry as a dot product of $\overrightarrow{Ga_j}$ and $\overrightarrow{k_j}$. This quantity is presented as "Ga dose (SEM)" in Table 1. Based on this geometric information, angles and distances measured in the SEM image and the fact that the nanowire is a right hexagonal prism, the 3D geometric information about the wire can be calculated based on this 2D SEM micrograph. This is indeed necessary for the correction of EDS profiles, as the TEM lamellas are not cut perpendicularly to the wire axis.

Table 1: Summary of the data for the V_O-rich sample, extracted from EDS characterization and gallium diffusion model, both presented above. In total, six (independent) facets from two ZnO wires were characterized. *Ga dose* represents the amount of deposited gallium relative to deposition onto a facet perpendicular to Ga flux. It is calculated based on the geometrical setup of the apparatus and the sample. *Effective Ga dose Q* was extracted from the diffusion model based on fitted Ga profiles and calibrated with the Ga dose value 0.77 for B facet of Wire-2. This is used as a common reference for both wires. *Diffusion length λ* and *diffusion coefficient D* are extracted from the diffusion model. All of the values are based on the corrected EDS data.

Wire	Facet	Ga dose (SEM)	Effective Ga dose Q (EDS fit)	Diffusion length λ (nm)	Diffusion coefficient D ($m^2 \cdot s^{-1}$)	Comment
2	A	0.08	0.26	44	$4.4 \cdot 10^{-19}$	low direct Ga deposition
2	B	0.77 **(ref.)**	0.77	120	$32.1 \cdot 10^{-19}$	affected by AES measurement
2	C	0.55	0.45	107	$25.6 \cdot 10^{-19}$	affected by AES measurement
1	D	0.87	0.55	75	$12.5 \cdot 10^{-19}$	
1	E	0.88	0.23	50	$5.7 \cdot 10^{-19}$	
1	F	0.00	0.08	39	$3.4 \cdot 10^{-19}$	no direct Ga deposition

The EDS elemental maps acquired from Wire-2 lamella together with the HAADF image are presented in Fig. 18. (The EDS characterization was performed on ThermoFisher Talos F200i S/TEM microscope with Dual-X detectors.) The information of utmost importance is that gallium *does* penetrate into the ZnO wire, see Fig. 18a. This proves that the procedure used is applicable for the incorporation of gallium into ZnO, potentially leading to high doping levels. However, gallium is distributed inhomogeneously in two distinct ways:

- (i) Its concentration is higher near the wire surface and decreases towards the nanowire central axis. This is not surprising; it indicates a diffusive process that was stopped before the homogeneous concentration could be reached. Longer annealing shall be applied for a more homogeneous Ga distribution. Another possibility – increasing the annealing temperature – is not recommended as it would promote the decomposition of ZnO (as discussed above).
- (ii) As can be seen in the Ga EDS map, there are brighter and darker spots and lines even for the same distance from the wire surface. This adds another level of inhomogeneity. (This will be further discussed for gallium depth-profiles extracted from this map, see Fig. 19c. The profiles are not monotonous near the surface in particular.) This points to strong surface effects having an impact; in particular, the ZnO decomposition (formation of etched-away

pits on the surface) may play a role. Another fact that supports the presence of surface effects is the deficiency of Zn in the vicinity of wire facets – compare the EDS maps of zinc and oxygen and see the combined image in Fig. 18. These surface-related inhomogeneity effects are more pronounced on sidewall facets where more gallium was deposited (i.e. the top-left and the top-right facet in the view of Fig. 18, as opposed to the left facet – inferred from the inset SEM micrograph). This is in line with the previous conclusion that the decomposition of the ZnO surface is gallium-induced (see the AES results discussion above).

Based on these findings, more optimal experimental conditions will require lower annealing temperature (to prevent ZnO decomposition) and longer annealing time to counterbalance the decreased temperature and to promote more homogeneous gallium distribution within the wire.

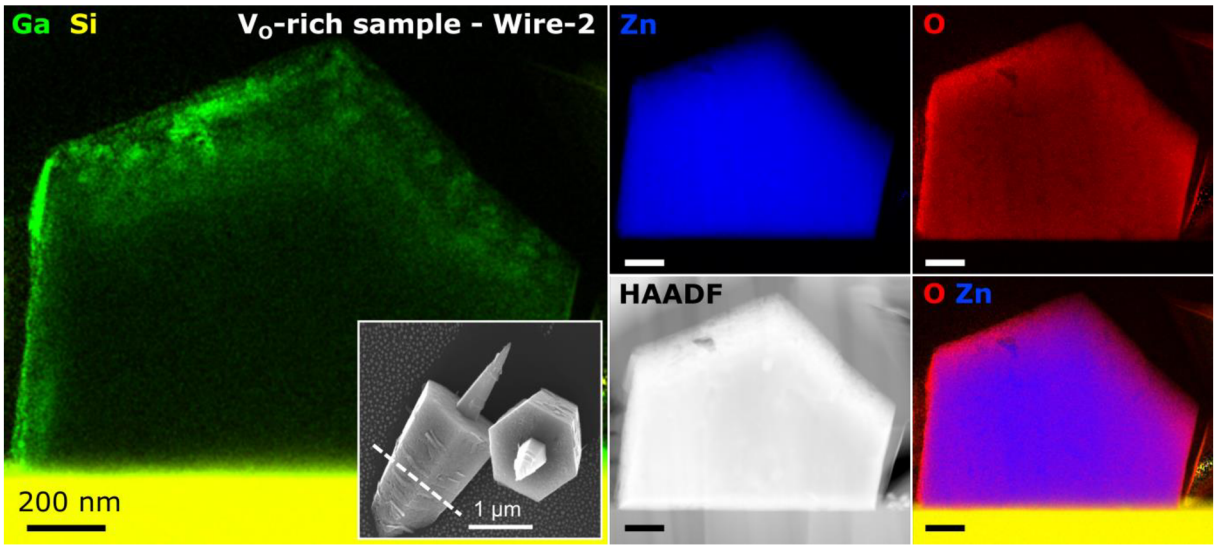

Fig. 18: STEM EDS maps of Wire-2 lamella from the V_O-rich sample. The location of the lamella (cut perpendicularly to the growth substrate) is shown in the inset (SEM top view, white dashed line) and also in Fig. 17a. Results for Ga, Si, Zn and O elements are presented, together with HAADF image and combined O+Zn map. Imaging: K. Bukvišová. Data analysis: author of the thesis.

The depth-profiles extracted from the EDS maps will be presented and discussed hereafter. In Fig. 19a, the positions of line spectra of Wire-2 are indicated for sidewall facets labelled A, B and C. The EDS map was pre-filtered by applying 3px-averaging. The line spectra are integrated over a 100px-wide area (indicated by the dotted lines of the same colour, see the schematics). The as-measured EDS spectra and HAADF signal for the B facet (i.e. measured along the red dashed line indicated in Fig. 19a) are shown in Fig. 19b for illustration. The bottom graph ibid. (showing gallium profile) is a zoomed-in detail of the upper graph.

For the correct interpretation of the EDS depth-profiles, the correction dealing with nanowire geometry with respect to the plane of TEM lamella is needed. Having applied the correction, graphs in Fig. 19c,d,e show the EDS depth-profiles of gallium, zinc and oxygen in the ZnO wire, going from its surface inwards. The measurements were done on three independent facets with different Ga dose deposited. The highest Ga dose was deposited onto the B facet, less onto the C facet and the least onto the A facet (see Table 1 for the exact values). The depth-profiles are compared directly for all facets, see the Figure.

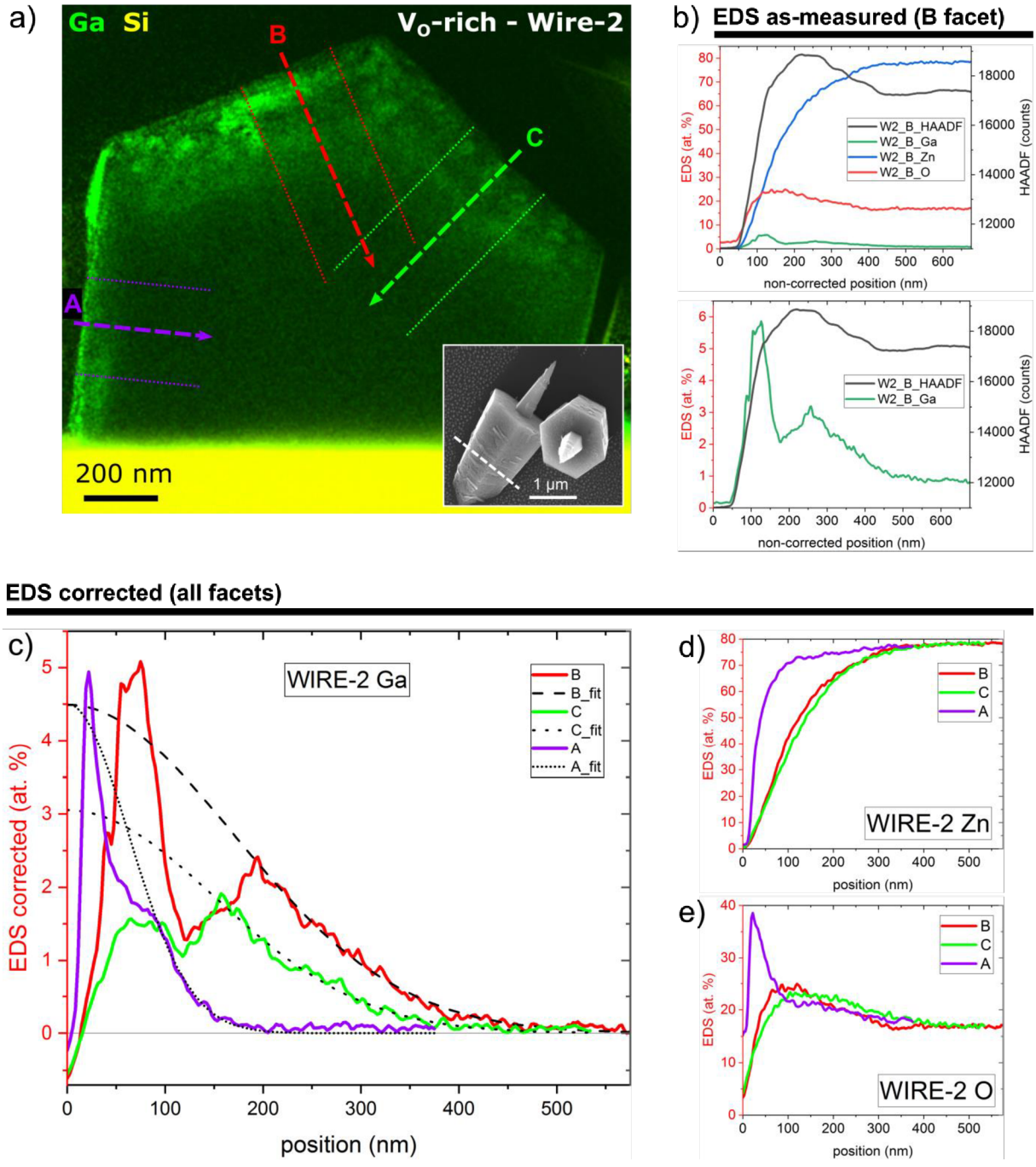

Fig. 19: ZnO Wire-2 (V_O-rich sample) EDS profiles. a) EDS map of Ga (green) acquired from the inclined cross-sectional TEM lamella. The location of the lamella within the wire is shown in the inset (take notice of the wire facets). The position of the elemental line profiles (perpendicular to lamella's edges) is indicated by coloured dashed lines (purple, red and green for the A, B and C edge, respectively). The line spectra are integrated over a 100px-wide area, indicated by the dotted lines of the same colour. b) To illustrate the data handling, the as-measured line spectra of the B profile are shown for Ga, Zn, O and HAADF signal. No correction is applied yet (see explanation in the text). The lower graph in b) shows a zoomed-in Ga spectrum from the upper graph. c,d,e) Corrected EDS depth-profiles of gallium, zinc and oxygen, respectively. After necessary corrections described in the text, the spectra represent real depth-profiles, perpendicular to nanowire sidewall facets A, B and C. The black dashed/dotted lines in c) show the Ga concentration profiles extracted from the diffusion model for A, B and C facets. (Note a good fit for the inner part of the profiles.) Also, pay attention to different colour-coding of the b) figure, which corresponds to the EDS maps shown in Fig. 18. In contrast, the colour-coding of c-e) reflects the schematics in figure a).

For gallium profiles presented in Fig. 19c, it is clear that a substantial amount of gallium incorporates up to several hundreds of nm inside the wire. The penetration depth increases with the original Ga dose. Also, double-peak behaviour is observed for all the facets. The first maximum belongs to gallium trapped on or near the surface. The other maximum is due to Ga diffusing into the volume of the wire – therefore it is much more informative and valid for the assessment of diffusional incorporation of Ga into ZnO wires. This inner part of the depth-profiles (i.e. neglecting the part close to the wire surface) will be further incorporated into a simple diffusion model, see below. Regarding Zn profiles in Fig. 19d, a clear Zn deficiency near the surface area is seen for B and C facets, which are the ones with higher Ga dose deposited. This result corresponds to the EDS maps presented in Fig. 18.

Generally, the gallium diffusion process follows Fick's second law, for 1D case being

$$\frac{\partial \varphi(x,t)}{\partial t} = D \cdot \frac{\partial^2 \varphi(x,t)}{\partial x^2}, \tag{3.1}$$

where $\varphi(x,t)$ is Ga concentration and $D = const.$ is the diffusion coefficient of Ga in ZnO for a given temperature T. (Keep in mind the dependence $D = D_0 \cdot e^{-\frac{E_a}{kT}}$. In case of another experiment performed at a different temperature, the activation energy of diffusion E_a and coefficient D_0 could be determined from the Arrhenius plot.) Solution of Fick's second law for limited-source diffusion – which is our case with a finite Ga dose deposited onto the ZnO wire – can be written in the following form [55]:

$$\varphi(x,t) = \frac{Q}{\sqrt{2Dt} \cdot \sqrt{2\pi}} \cdot e^{-\frac{x^2}{2\left(\sqrt{2Dt}\right)^2}}, \tag{3.2}$$

which happens to be a Gaussian function of a normal distribution centred at zero (i.e. at the wire surface). Its standard deviation equals $\sqrt{2Dt}$. Let's define the diffusion length as $\lambda = \sqrt{Dt}$. The quantity Q represents the amount of gallium deposited on the facet; it will be called *effective Ga dose* in further text. It can be understood as the area below the concentration profile.

For each Ga profile in Fig. 19c, the inner part (neglecting the part near the wire surface due to reasons presented above) was fitted with equation (3.2) of the diffusion model and plotted into the graph as dashed and dotted black lines – see ibid. The annealing time t of 4500 s (i.e. the duration of annealing at the highest temperature, 480 °C) is considered for all facets. (The time needed to reach the final temperature is not considered for simplicity.) Based on the fitted curves, the following quantities are calculated individually for each facet: (i) effective Ga dose Q, (ii) diffusion length λ and (iii) diffusion coefficient D. The results are summarized in Table 1 (together with the results for Wire-1 from the same sample, discussed further below). Comparing the effective Ga dose with the dose calculated geometrically, there are some variations; however, the trend is similar. Also, the diffusion length differs for the three facets – ranging from 44 nm to 120 nm. The diffusion coefficient varies accordingly. However, the exact numbers are not that important here. What matters is the overall magnitude of the diffusion coefficient D – lying within one order of magnitude.

Nearly identical conclusions to those just discussed for Wire-2 can be drawn for the other wire (i.e. Wire-1) as well. Its EDS maps are presented in Fig. 20. Keep in mind that the two wires are from the same V_O-rich sample and have therefore undergone the same experimental procedure. There is one exception though – Wire-1 was *not* characterized by SEM/AES techniques at elevated temperature

before the EDS measurements. Another difference between the wires is the amount of deposited gallium on individual facets – it is different for each facet of each wire due to their unique geometric orientation relative to the incoming Ga flux.

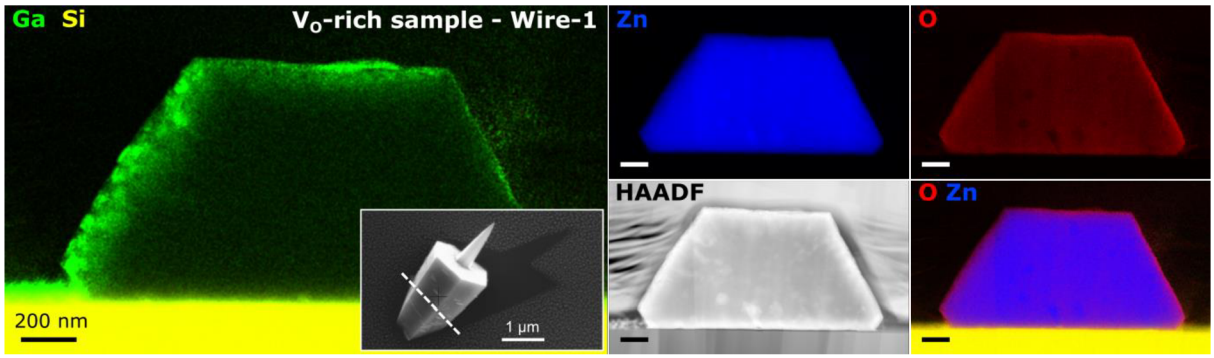

Fig. 20: STEM EDS maps of Wire-1 lamella (taken from the V_O-rich sample). The location of the lamella (cut perpendicularly to the growth substrate) is shown in the inset (SEM top view, white dashed line) and also in Fig. 17b. Results for Ga, Si, Zn and O elements are presented, together with the HAADF image and combined O+Zn map. Imaging: K. Bukvišová. Data analysis: author of the thesis.

The same data processing as described above was applied to the EDS maps of Wire-1 lamella presented in Fig. 20. Location of the EDS depth-profiles on three distinct Wire-1 facets (labelled D, E, F) is presented in Fig. 21a. The unprocessed (non-corrected) EDS and HAADF spectra of the D facet are shown in Fig. 21b for illustrative purposes. More importantly, the corrected depth-profiles of Ga, Zn and O are depicted in Fig. 21c,d,e, respectively. The surface effects affecting the gallium profiles are much weaker, which is in line with the profiles' much more predictable behaviour. Apart from that, the qualitative conclusions are the same as for Wire-2 discussed above. Regarding the numerical values, see the summary for both wires in Table 1.

Two comments are worth pointing out:

- There was no direct deposition of Ga onto the F facet of Wire-1 (due to geometric setup). Still, the depth-profile in Fig. 21c shows a certain amount of gallium penetrating from this facet into the wire (see the purple profile). This can be explained by the surface diffusion of gallium from the E facet onto the F facet at first (when the temperature has been raised), followed by gallium incorporation. Indeed, both the effective Ga dose (thus being positive) and the diffusion length for the F facet are the smallest among all facets inspected – see the exact figures in Table 1.
- (ii) The range of Ga diffusion length for the Wire-1 facets (39 nm – 75 nm) is much narrower than for Wire-2 (44 nm – 120 nm) and the diffusion length is generally smaller. Together with the fact that the Ga depth-profiles of Wire-1 show smaller surface effects (including one maximum only), this indicates that the AES characterization of Wire-2 could have indeed influenced Ga incorporation by local heating of the B and C facets most exposed to the electron beam. Note that these facets show the highest diffusion length (120 nm and 107 nm) – a factor of 2 to 3 higher than the rest of the facets. Therefore, it is Wire-1 that is considered a more valid and credible reference for other measurements (e.g. the H_2O_2-preannealed wire presented below) or further research.

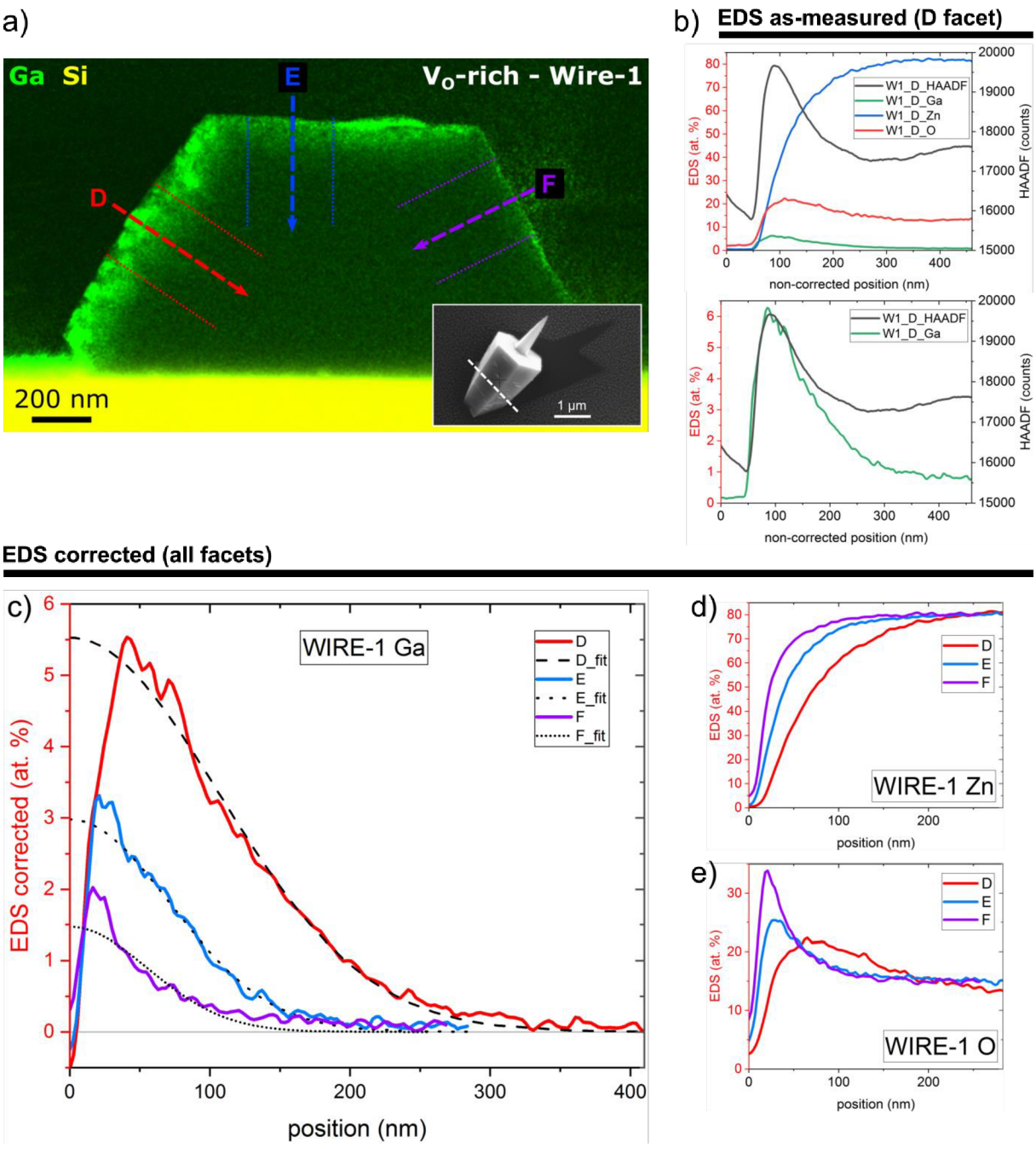

Fig. 21: ZnO Wire-1 (V_O-rich sample) EDS profiles. (The data layout is the same as in Fig. 19 for Wire-2). a) EDS map of Ga (green) acquired from the inclined cross-sectional TEM lamella. The location of the lamella within the wire is shown in the inset (take notice of the wire facets). The position of the elemental line profiles (perpendicular to lamella's edges) is indicated by coloured dashed lines (red, blue and purple for the D, E and F edge). The line spectra are integrated over a 100px-wide area, indicated by the dotted lines of the same colour. b) To illustrate the data handling, the as-measured line spectra of the D profile are shown for Ga, Zn, O and HAADF signal. No correction is applied yet (see explanation in the text). The lower graph in b) shows a zoomed-in Ga spectrum from the upper graph. c,d,e) Corrected EDS depth-profiles of gallium, zinc and oxygen, respectively. After necessary corrections described in the text, the spectra represent real depth-profiles, perpendicular to nanowire sidewall facets D, E, F. The black dashed/dotted lines in c) show the Ga concentration profiles extracted from the diffusion model for the D, E and F facets. Pay attention to different colour-coding of b) figure, which corresponds to the EDS maps shown in Fig. 20. In contrast, the colour-coding of c-e) reflects the schematics in fig a).

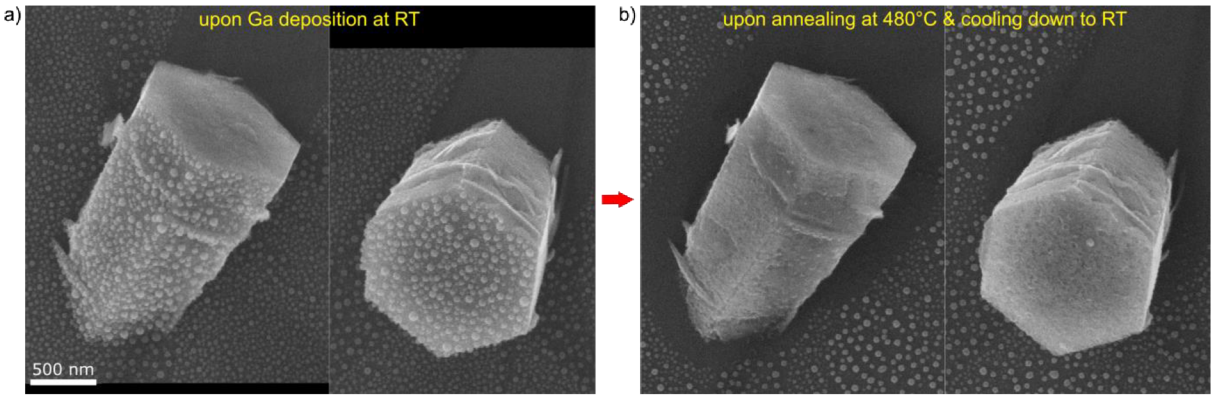

Fig. 22: SEM micrographs of the V_O-poor (i.e. H_2O_2-preannealed) ZnO wires taken a) upon Ga deposition at room temperature, b) upon subsequent in-situ annealing (480 °C, 75 min) and cooling down to room temperature for SEM imaging. Similarly to V_O-rich (i.e. vacuum-preannealed) ZnO wires (see Fig. 15), the annealing step induced Ga incorporation into ZnO wires and Ga-induced ZnO decomposition. The decomposition takes place only on areas originally decorated with gallium.

The EDS results for the V_O-rich nanowires presented above are to be compared with a V_O-poor ZnO nanowire. Its preparation was the same as for the V_O-rich sample except for the pre-annealing step, which was performed in H_2O_2 gas (30 min, 300 °C, 6 kPa) instead of vacuum. SEM images of selected nanowires before and after the final annealing step are shown in Fig. 22. SEM results regarding morphological changes are the same as for the V_O-rich nanowire: Gallium droplets on the decorated facets got consumed and the facets show rough morphology. The facets without gallium remained smooth and intact. Hence the gallium-induced decomposition of ZnO has been shown for this sample as well.

Further, a TEM lamella was cut from another nanowire for EDS inspection. The same procedures were used as for the V_O-rich sample presented above. SEM image of the nanowire and location of the lamella are shown in the inset of Fig. 23. The EDS elemental maps and HAADF image are presented in the same Figure. The top-left and top-right sidewall facets were originally decorated with gallium. Clearly, Ga gets incorporated in a considerably inhomogeneous way – being located mostly at/near the wire surface and within the subsurface clusters. These clusters are probably correlated with the pores and hollows in nanowire sidewalls – see the rough surface morphology in Fig. 22b. This effect could be inhibited by applying lower annealing temperature (450 °C or less, as proved sufficient for Ga incorporation based on real-time SEM analysis shown in Fig. 15). However, for the sake of direct comparison, both V_O-rich and V_O-poor samples were annealed at the same temperature 480 °C for the same time of 4500 s. Similarly to the V_O-rich wires, weaker Zn signal is observed near the wire surface (see combined O+Zn image in Fig. 23) and it also correlates with stronger Ga signal (better seen in the EDS line spectra shown below, see e.g. the Ga protrusion on the G profile – compare blue spectra of Ga and Zn in Fig. 24c,d).

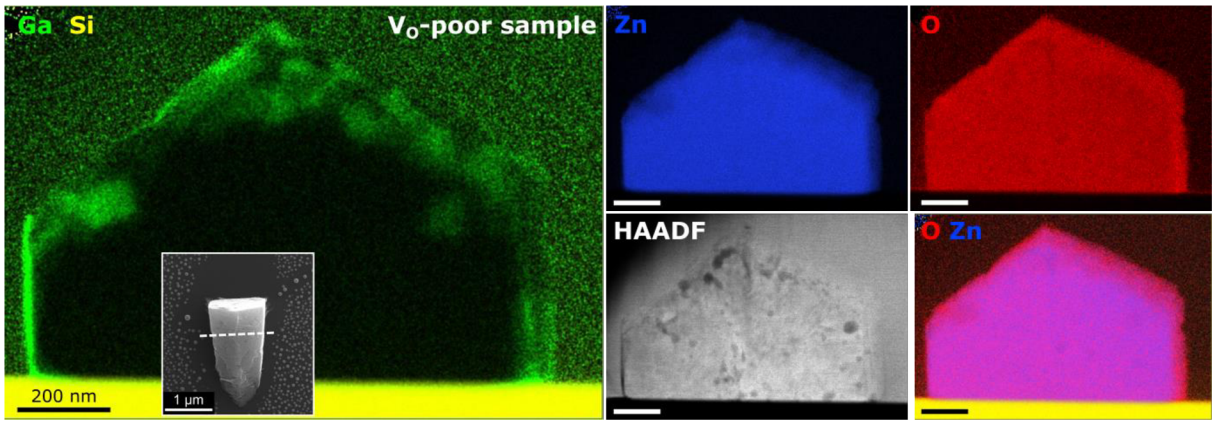

Fig. 23: STEM EDS maps of nanowire lamella taken from the V_O-poor sample. The location of the lamella (cut perpendicularly to the growth substrate) is shown in the inset (SEM top view, white dashed line). Results for Ga, Si, Zn and O elements are presented, together with the HAADF image and combined O+Zn map. Imaging: K. Bukvišová. Data analysis: author of the thesis.

The depth-profiles extracted from the EDS maps are presented in Fig. 24. Positions of the line spectra are indicated in Fig. 24a – labelled G, H and J. The EDS maps were pre-filtered by applying 3px-averaging. The line spectra are integrated over a 60px-wide area (indicated by dotted lines of the same colour). The as-measured (i.e. non-corrected) EDS spectra and HAADF signal for the H line are shown in Fig. 24b for illustration. The bottom graph ibid. (showing gallium profile) is a zoomed-in detail of the upper graph. The corrected depth-profiles of Ga, Zn and O are depicted in Fig. 24c,d,e, respectively. The same correction procedure as for the V_O-rich sample was used.

The positions of line spectra G and J were chosen on purpose, in order to show Ga-rich protrusions within the nanowire. However, homogeneous gallium incorporation is of more interest. Therefore, the H profile is studied further, as it covers the most homogeneous region of the lamella. Ga signal of H profile was fitted with the diffusion model presented earlier – see the black dashed line in Fig. 24c. The surface-affected area (marked with dotted line ibid., corresponding well to the projection of wire surface into the lamella plane due to the finite width of TEM lamella) was not considered in the fitting procedure. Annealing time t of 4500 s (duration of annealing at the highest temperature, 480 °C) was used as an input. Based on the fitted curve, diffusion length λ and diffusion coefficient D are calculated and summarized in Table 2 – for the purpose of comparing the V_O-rich nanowire (Fig. 21) with the V_O-poor one (Fig. 24). From the V_O-rich sample, Wire-1 was selected as more representative due to the reasons discussed above. Further, facet F was discarded, as there had been no direct Ga deposition on that facet, thus being unrepresentative for Ga incorporation evaluation.

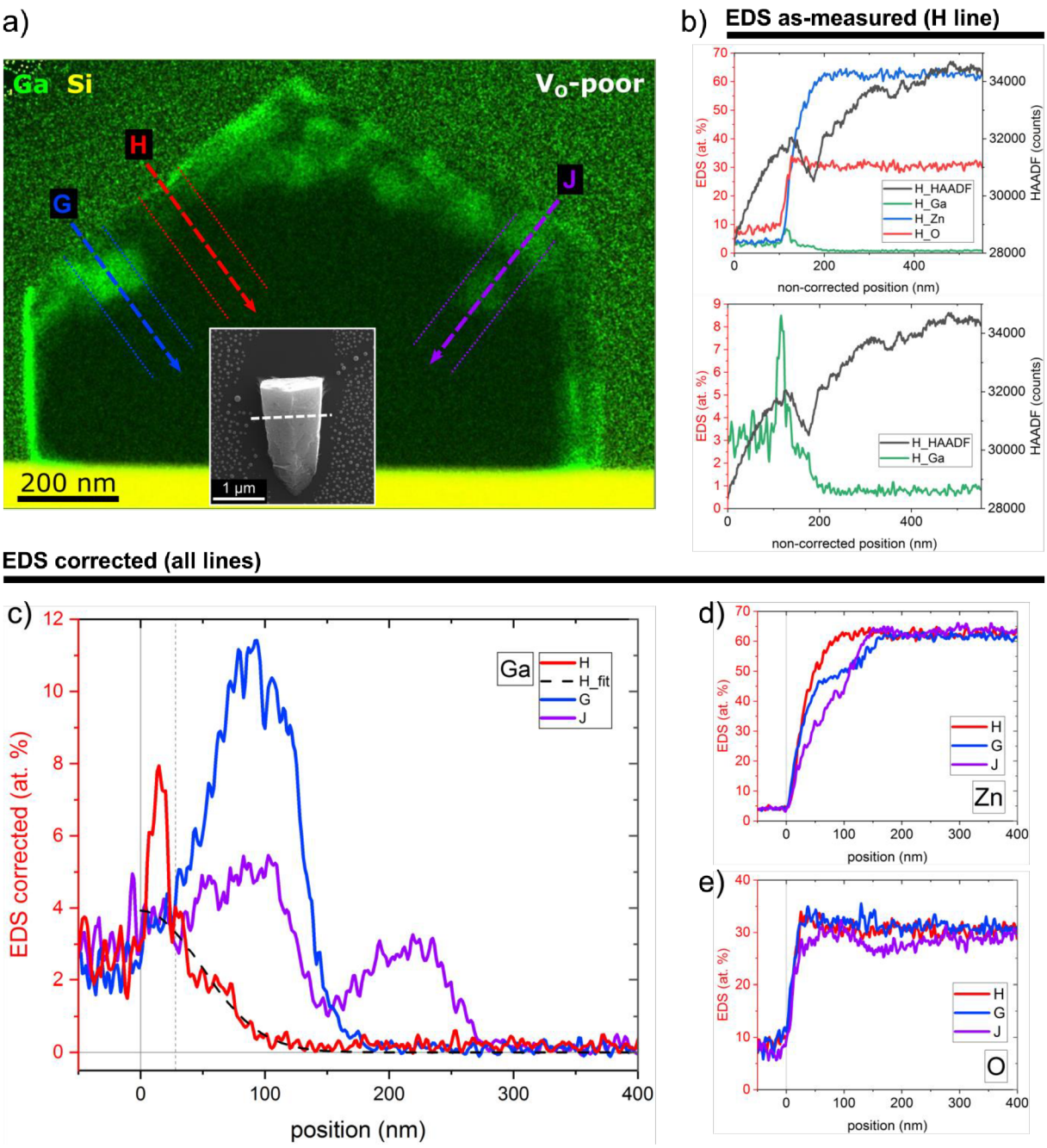

Fig. 24: EDS profiles of the V_O-poor nanowire. a) EDS map of Ga (green) acquired from the inclined cross-sectional TEM lamella (see its location in the SEM top-view inset). The position of the elemental line profiles (perpendicular to lamella's edges) is indicated by the coloured dashed lines. The line spectra are integrated over a 60px-wide area, indicated by the dotted lines of the same colour. b) For illustration, the as-measured line spectra of the H profile are shown for Ga, Zn, O and HAADF signal. No correction is applied yet. The lower graph in b) shows a zoomed-in Ga spectrum from the upper graph. c,d,e) Corrected EDS depth-profiles of gallium, zinc and oxygen, respectively. After the corrections described in the text, the spectra represent real depth-profiles, perpendicular to nanowire sidewall facets. In fig. c), the grey dotted vertical line (serving as a guide to the eye) separates the surface-influenced region of the H profile, which is not considered in the diffusion model. The black dashed line in c) shows the Ga concentration profile extracted from the diffusion model for H measurement. Beware of the different colour-coding of b) figure, which corresponds to the EDS maps shown in Fig. 23. In contrast, the colour-coding of c-e) reflects the schematics in fig a).

Table 2: Comparison of the data extracted from EDS characterization and gallium diffusion model for V_O-rich and V_O-poor ZnO nanowire. *Ga dose* represents the amount of gallium deposited onto the sidewall relative to deposition onto an imaginary facet perpendicular to Ga flux. It is calculated based on the geometrical setup of the apparatus and the sample. *Diffusion length λ* and *diffusion coefficient D* are extracted from the diffusion model. All of the values are based on the corrected EDS data.

Wire	Facet	Ga dose (SEM)	Diffusion length λ (nm)	Diffusion coefficient D ($m^2 \cdot s^{-1}$)
V_O-rich sample (Wire-1)	D	0.87	75	$12.5 \cdot 10^{-19}$
V_O-rich sample (Wire-1)	E	0.88	50	$5.7 \cdot 10^{-19}$
V_O-poor sample	H	0.60	34	$2.6 \cdot 10^{-19}$

Comparing the EDS results of V_O-rich and V_O-poor ZnO nanowires leads to the following conclusions:

- Weaker Zn signal correlates with stronger Ga signal for both samples, being an indication of substitutional doping.
- Gallium incorporation is stronger and way more homogeneous for the V_O-rich ZnO nanowire (compare Fig. 21 and Fig. 24). Also, note the sharp boundary between Ga protrusions and ZnO material in the V_O-poor sample (well seen in G profile), further indicating that low concentration of oxygen vacancies inhibits Ga diffusion into ZnO.
- Gallium diffusion length in ZnO, as well as the diffusion coefficient, is larger for the V_O-rich nanowire (by a factor of 1.5 to 2.2 for λ; by a factor of 2.2 to 4.8 for D, see Table 2). Note however that this quantification serves as a rough estimate for drawing qualitative conclusions. In order to perform a quantitative study, more samples shall be inspected and surface effects would need to be considered in more detail.

To summarize, Ga diffusional doping of ZnO nanowires has been proved. The pre-annealing environment (vacuum or H_2O_2 gas) indeed influences Ga incorporation into ZnO. Most probably, oxygen vacancies (prepared by vacuum-preannealing) promote higher gallium diffusion into the ZnO material. On the contrary, pre-annealing in H_2O_2 gas decreases the concentration of oxygen vacancies, thus suppressing Ga diffusion, which is then limited to ZnO crystal imperfections.

One of the thesis goals was to assess the Ga diffusional-doping procedure for ZnO nanowires, with respect to achieving high doping levels needed for novel applications. The suitability of this method was proved by the EDS measurements, showing successful gallium incorporation – with concentration up to several at.% in the subsurface regions (5 at.% for V_O-rich sample, 3 at.% for V_O-poor sample). Such measurements correspond to Ga concentration in the range of $2 \cdot 10^{21}$ cm^{-3} – $4 \cdot 10^{21}$ cm^{-3}, well suitable for plasmonics and bio-sensing applications. For practical use, way more homogeneous gallium distribution would be needed, yet this is feasible by prolonged annealing time. As a proof-of-concept, the diffusional-doping method used was shown to be a viable option for achieving high doping levels of gallium in ZnO nanowires.

4 Conclusion

The research presented within the thesis was focused on the growth and in-depth characterization of germanium and zinc oxide semiconducting nanowires, with the intention of acquiring high doping levels.

Ge nanowires

Firstly, two elements of Ge nanowires' growth mechanism were studied in section 2.1 – the material transfer from the Au catalyst onto the nanowire and the impact of adsorbates passivating the sidewalls (atomic hydrogen in particular) onto nanowire growth and morphology. The experiments were performed either in vacuum conditions or with the assistance of atomic hydrogen, leading to dissimilar nanowire morphologies. The combined effect of atomic hydrogen adsorption and Au catalyst spreading on the growth direction and morphology was revealed and explained: It was shown that gold (diffusing out of the catalyst particle) promotes the formation of {111}-oriented sidewall facets, thus confining the nanowire growth into <110> direction. However, atomic hydrogen (if adsorbed on nanowire sidewalls) prevents gold from diffusing out of the catalyst. The nanowires then exhibit nearly cylindrical or hexagonal cross sections, as the growth is not constrained by any preferential sidewall orientation. Moreover, these results bridge the gap between the MBE and CVD growth methods, explaining their contradictory results – regarding nanowire growth direction in particular. The findings presented in the thesis bring additional insight into the explanation of Ge nanowire growth mechanism in general, highlighting the importance of surface adsorbates – being present on purpose (MBE setup) or unintentionally (most of the CVD methods, where hydrogen-containing adsorbates are generated as a by-product).

Secondly, Ge nanowire growth using dopant-containing catalysts was investigated in section 2.2 – with the intention of catalyst incorporation leading to nanowire doping. The alloyed Au–Ga catalyst was prepared and imaged in-situ during formation, followed by the successful growth of Ge nanowires – although the catalyst stability is lower than for pure Au. The presence of gallium in the catalyst atop the nanowire was confirmed by Auger electron spectroscopy and STEM EDS analysis. However, gallium incorporation from the catalyst into the nanowire was not observed. Growth from alloyed Au–In catalyst was successful, leading to in-plane Ge nanowires on (110)-oriented Ge wafer. To summarize, only the alloyed Au–Ga catalyst was found to be applicable for germanium out-of-plane nanowire growth. Despite high dopant concentration in the catalyst, no gallium incorporation into the nanowire was reached. Hence, this method of nanowire doping was proved unsuitable for the material system selected.

ZnO nanowires

Thirdly, the development of a procedure for high-level doping of ZnO nanowires was described in chapter 3. ZnO nanowires utilized for our experiments were grown via the AACVD method (aerosol-assisted CVD), more details of which were introduced in section 3.1. The impact of nanowire annealing in various environments on the concentration of oxygen vacancies was demonstrated based on XPS measurements, see section 3.2. Annealing in H_2O_2 gas substantially decreases the concentration of O vacancies in ZnO, compared to annealing in high vacuum.

Further, the procedure for diffusional doping of nanowires with gallium was described in section 3.3. The process of Ga incorporation into ZnO nanowires during annealing was documented in-situ in real

time in the SEM/AES apparatus. The decrease in volume of deposited gallium (indicating its incorporation into zinc oxide) was evident already at 350 °C. Having increased the temperature to 450 °C, gallium completely incorporated and smooth ZnO facets were seen. When further increasing the annealing temperature, gallium-induced decomposition of ZnO nanowires was observed. This leads to the formation of etched-away pits on nanowires' facets on areas of previous Ga deposition; regardless of the pre-annealing conditions. The evidence for distinguishing between ZnO thermal decomposition as such and Ga-induced process was shown and discussed. (Bare ZnO nanowires were stable up to 535 °C at least, when annealed in vacuum.)

Next, the STEM EDS characterization of nanowire cross-sectional lamellas is presented. The extent of Ga incorporation was studied for two distinct samples (with a high and a low concentration of oxygen vacancies, labelled V_O-rich (vacuum-preannealed) and V_O-poor (H_2O_2-preannealed), respectively) – in order to correlate Ga diffusion and the concentration of oxygen vacancies in the nanowires. Furthermore, a model for gallium diffusion into ZnO nanowires was implemented. Based on the diffusion model and EDS line spectra, diffusion coefficient and diffusion length were calculated for each sample. For both samples, a stronger Ga signal correlates with a weaker Zn signal, indicating substitutional doping. Gallium incorporation into ZnO nanowires was proved for both samples. For the V_O-rich sample, the diffusion coefficient of gallium in ZnO (and hence the diffusion length as well) is larger than for the V_O-poor sample. Also, the spatial distribution of Ga is more homogeneous within the V_O-rich nanowire.

To summarize, diffusional doping of ZnO nanowires with Ga was demonstrated and the suitability of various methods for doping-level analysis was assessed. The pre-annealing environment influences Ga incorporation into ZnO nanowires. The oxygen vacancies generated by vacuum-preannealing most likely promote higher and more homogenous gallium diffusion into ZnO material. By contrast, pre-annealing in H_2O_2 gas (which decreases the concentration of oxygen vacancies), suppresses Ga diffusion compared to oxygen-vacancy rich nanowires. Based on the EDS measurements, gallium concentration as high as $4 \cdot 10^{21}$ cm^{-3} was reached in the subsurface region of the V_O-rich ZnO nanowire and up to $2 \cdot 10^{21}$ cm^{-3} for the V_O-poor nanowire. Hence, the suitability of the presented diffusional-doping method for achieving high Ga doping levels in ZnO nanowires was demonstrated. Provided that Ga concentration homogeneity is improved by prolonged annealing time and the dopant activation is sufficient, the doping-method presented above is a viable option for reaching high doping levels of ZnO nanowires (in the order of 10^{21} cm^{-3}) needed for prospective applications, such as bio-sensing in the IR region.

References

1. **Hayden, O. et al.** *Nano Today.* 2008, Vol. 3, 5-6, p. 12. https://doi.org/10.1016/S1748-0132(08)70061-6.

2. **Chou, L.-W. et al.** *ACS Nano.* 2015, Vol. 9, 2, p. 1250. https://doi.org/10.1021/nn504974z.

3. **Naik, V. G. et al.** *Advanced Materials.* 2013, Vol. 25, 24, p. 3264. https://doi.org/10.1002/adma.201205076.

4. **Khurgin, J. and Boltasseva, A.** *MRS Bulletin.* 2012, Vol. 37, 8, p. 768. https://doi.org/10.1557/mrs.2012.173.

5. **Amit, I. et al.** *Nano Lett.* 2013, Vol. 13, 6, p. 2598. https://doi.org/10.1021/nl4007062.

6. **Perea, D. E. at al.** *Nature Nanotechnology.* 2009, Vol. 4, p. 315. https://doi.org/10.1038/nnano.2009.51.

7. **Connel, J. G. et al.** *Nano Lett.* 2013, Vol. 13, 1, p. 199. https://doi.org/10.1021/nl3038695.

8. **Erwin, S. et al.** *Nature.* 2005, Vol. 436, p. 91. https://doi.org/10.1038/nature03832.

9. **Moutanabbir, O. et al.** *Nature.* 2013, Vol. 496, p. 78. https://doi.org/10.1038/nature11999.

10. **Chen, W. et al.** *Nature Communications.* 2014, Vol. 5, p. 1. https://doi.org/10.1038/ncomms5134.

11. **Kolíbal, M. et al.** *Appl. Phys. Lett.* 2011, Vol. 99, 14, p. 143113. https://doi.org/10.1063/1.3647774.

12. **Kolíbal, M. et al.** *Appl. Phys. Lett.* 2012, Vol. 100, 20, p. 203102. https://doi.org/10.1063/1.4714765.

13. **Kolíbal, M. et al.** *Nano Lett.* 2014, Vol. 14, 4, p. 1756. https://doi.org/10.1021/nl404159x.

14. **Sivaram, S. V. et al.** *J. Am. Chem. Soc.* 2015, Vol. 137, 31, p. 9861. https://doi.org/10.1021/jacs.5b03818.

15. **Gamalski, A. D. et al.** *Nano Lett.* 2015, Vol. 15, 12, p. 8211. https://doi.org/10.1021/acs.nanolett.5b03722.

16. **Kolíbal, M. et al.** *Nano Lett.* 2016, Vol. 16, 8, p. 4880. https://doi.org/10.1021/acs.nanolett.6b01352.

17. **Briggs, D. and Grant, J. T.** *Surface Analysis by Auger and X-ray Photoelectron Spectroscopy.* s.l. : IM Publications and SurfaceSpectra Limited, 2003. ISBN: 1-901019-04-7.

18. **Porret, C. et al.** *J. Cryst. Growth.* 2011, Vol. 323, 1, p. 334. https://doi.org/10.1016/j.jcrysgro.2010.11.056.

19. **Dubrovskii, V. G. et al.** *Surface Science.* 2007, Vol. 601, 18, p. 4395. https://doi.org/10.1016/j.susc.2007.04.122.

20. **Gamalski, A. D. et al.** *J. Phys. Chem. C.* 2011, Vol. 115, 11, p. 4413. https://doi.org/10.1021/jp1095882.

21. **Ross, F. M. et al.** *Phys. Rev. Lett.* 2005, Vol. 95, 14, p. 146104. https://doi.org/10.1103/PhysRevLett.95.146104.

22. **Ryu, S.-G. et al.** *ACS Nano.* 2013, Vol. 7, 3, p. 2090. https://doi.org/10.1021/nn400186c.

23. **Cho, H. S. and Kamins, T. I.** *J. Cryst. Growth.* 2010, Vol. 312, 16-17, p. 2494. https://doi.org/10.1016/j.jcrysgro.2010.05.035.

24. **Wiethoff, C. et al.** *Nano Lett.* 2008, Vol. 8, 9, p. 3065. https://doi.org/10.1021/nl801146q.

25. **Hannon, J. B. et al.** *Nature.* 2006, Vol. 440, p. 69. https://doi.org/10.1038/nature04574.

26. **Stekolnikov, A. A. and Bechstedt, F.** *Phys. Rev. B.* 2005, Vol. 72, 12, p. 125326. https://doi.org/10.1103/PhysRevB.72.125326.

27. **Su, C. et al.** *Surface Science.* 2000, Vol. 445, 2-3, p. 139. https://doi.org/10.1016/S0039-6028(99)00991-7.

28. **Akazawa, H. J.** *J. Appl. Phys.* 2006, Vol. 99, 10, p. 103505. https://doi.org/10.1063/1.2194232.

29. **Scholz, S. M. et al.** *Surface Science.* 1995, Vols. 331-333, p. 402. https://doi.org/10.1016/0039-6028(95)00297-9.

30. **Kamins, T. I. et al.** *Nano Lett.* 2004, Vol. 4, 3, p. 503. https://doi.org/10.1021/nl035166n.

31. **Nebol'sin, V. A. and Shchetinin, A. A.** *Inorganic Materials.* 2003, Vol. 39, 9, p. 899. https://doi.org/10.1023/A:1025588601262.

32. **Yu, L. et al.** *Appl. Phys. Lett.* 2011, Vol. 98, 12, p. 123113. https://doi.org/10.1063/1.3569817.

33. **Biswas, S. et al.** *Nature Communications.* 2016, Vol. 7, p. 11405. https://doi.org/10.1038/ncomms11405.

34. **Seifner, M. S. et al.** *Cryst. Growth Des.* 2019, Vol. 19, 5, p. 2531. https://doi.org/10.1021/acs.cgd.9b00210.

35. **Perea, D. E. et al.** *Nano Lett.* 2011, Vol. 11, 8, p. 3117. https://doi.org/10.1021/nl201124y.

36. **Wen, C.-Y. et al.** *Science.* 2009, Vol. 326, 5957, p. 1247. https://doi.org/10.1126/science.1178606.

37. **Kaufman, S. M. and Whalen, T. J.** *Acta Metallurgica.* 1965, Vol. 13, 7, p. 797. https://doi.org/10.1016/0001-6160(65)90144-6.

38. **Aqra, F. and Ayyad, A.** *Metallurgical and Materials Transactions A.* 2011, Vol. 42, p. 2680. https://doi.org/10.1007/s11661-011-0686-z.

39. **Kolíbal, M. et al.** *Nanotechnology.* 2018, Vol. 29, 20, p. 205603. https://doi.org/10.1088/1361-6528/aab474.

40. **Elliott, R. P. and Shunk, F. A.** *Bulletin of Alloy Phase Diagrams.* 1981, Vol. 2, 3, p. 356. https://doi.org/10.1007/BF02868293.

41. **Janotti, A. and Van de Walle, C. G.** *Rep. Prog. Phys.* 2009, Vol. 72, 12, p. 126501. https://doi.org/10.1088/0034-4885/72/12/126501.

42. **Ellmer, K. and Bikowski, A.** *J. Phys. D: Appl. Phys.* 2016, Vol. 49, 41, p. 413002. https://doi.org/10.1088/0022-3727/49/41/413002.

43. **Mauit, O. et al.** *Thin Solid Films.* 2019, Vol. 690, p. 137533. https://doi.org/10.1016/j.tsf.2019.137533.

44. **Li, F. et al.** *Nanoscale.* 2020, Vol. 12, 30, p. 16153. https://doi.org/10.1039/D0NR03740K.

45. **Agrawal, A. et al.** *Annu. Rev. Mater. Res.* 2017, Vol. 47, p. 1. https://doi.org/10.1146/annurev-matsci-070616-124259.

46. **Vallejos, S. et al.** *ACS Appl. Mater. Interfaces.* 2016, Vol. 8, 48, p. 33335. https://doi.org/10.1021/acsami.6b12992.

47. **Vallejos, S. et al.** *Proceedings.* 2017, Vol. 1, 4, p. 417. https://doi.org/10.3390/proceedings1040417.

48. **Mikula, M.** Příprava nanodrátů pro fotoniku. 2019. Brno: Vysoké učení technické v Brně, Fakulta strojního inženýrství. (Diploma thesis. Supervisor: doc. Ing. Miroslav Kolíbal, PhD.).

49. **Namgung, G. et al.** *ACS Appl. Mater. Interfaces.* 2019, Vol. 11, 1, p. 1411. https://doi.org/10.1021/acsami.8b17336.

50. **Gabás, M. et al.** *J. Appl. Phys.* 2013, Vol. 113, 16, p. 163709. https://doi.org/10.1063/1.4803063.

51. **Park, S.-M. et al.** *Thin Solid Films.* 2006, Vol. 513, 1-2, p. 90. https://doi.org/10.1016/j.tsf.2006.01.051.

52. **Das, D. and Mondala, P.** *RSC Adv.* 2016, Vol. 6, 8, p. 6144. https://doi.org/10.1039/C5RA22288E.

53. **Fan, J. C. C. and Goodenough, J. B.** *J. Appl. Phys.* 1977, Vol. 48, 8, p. 3524. https://doi.org/10.1063/1.324149.

54. **El-Shaer, A. et al.** 2005, Vol. 38, 4-6, p. 265. https://doi.org/10.1016/j.spmi.2005.08.025.

55. **Kasap, S. and Capper, P.** *Springer Handbook of Electronic and Photonic Materials.* s.l. : Springer International Publishing, 2017. ISBN: 978-3-319-48931-5.

Author's publications and conference contributions

Publications in impact journals

- Kolíbal M., **Pejchal T.**, Vystavěl T., Šikola T.: The synergic effect of atomic hydrogen adsorption and catalyst spreading on Ge nanowire growth orientation and kinking. *Nano Letters* 2016, vol. 16, 8, p. 4880. [16]

  DOI: 10.1021/acs.nanolett.6b01352

  Impact factor (2016): 12.712

  My contribution:
  I have conducted the nanowire growth experiments in the vacuum chamber connected to the Auger Electron Spectroscopy system (AES). I have analyzed the nanowires with AES and ex-situ SEM and I have evaluated the results. I have been leading the discussions of the results with other authors and I have contributed to writing the manuscript.

- Kolíbal M., **Pejchal T.**, Musálek T., Šikola T.: Catalyst–substrate interaction and growth delay in vapor–liquid–solid nanowire growth. *Nanotechnology* 2018, vol. 29, 20, p. 205603. [39]

  DOI: 10.1088/1361-6528/aab474

  Impact factor (2018): 3.399

  My contribution:
  I have conducted the growth and catalyst-annealing experiments in the vacuum chamber connected to the Auger Electron Spectroscopy system (AES). I have analyzed the samples with AES and ex-situ SEM and I have evaluated the results. I have contributed to the discussions of the results with other authors and to writing the manuscript.

- **Pejchal T.**, Vallejos, S., Bukvišová K., Šikola, T., Kolíbal M.: Ga interaction with ZnO surfaces: diffusion and melt-back etching.

  To be submitted.

  My contribution:
  I have conducted the deposition, annealing and melt-back-etching experiments. I have analyzed the nanowires with SEM and AES, including the real-time imaging. I have evaluated the results including the XPS, TEM and EDS STEM analysis. I have been leading the discussions of the results with other authors and I have contributed to writing the manuscript.

Active conference contributions

- Nanowire Growth Workshop & Nanowires Workshop 2015
  26^{th} – 30^{th} October 2015, Barcelona, Spain

  Pejchal T., Kolíbal M., Šikola T.: *The role of hydrogen in Ge nanowire growth.* Poster presentation.

- NANOCON 2016 – 8^{th} International Conference on Nanomaterials - Research & Application
  19^{th} – 21^{st} October 2016, Brno, Czech Republic

  Pejchal T., Kolíbal M., Vystavěl T., Šikola T.: *The synergic of atomic hydrogen and catalyst spreading on Ge nanowire growth orientation and kinking.* Poster presentation.

- Nanowire Week 2017 – 10^{th} Nanowire Growth Workshop + 9^{th} Nanowires
  29^{th} May – 2^{nd} June 2017, Lund, Sweden

  Pejchal T., Musálek T., Šikola T., Kolíbal M.: *Group-III catalysts: Preparation and Ge nanowire growth.* Poster presentation.

- Austrian MBE Workshop 2017
  28^{th} – 29^{th} September 2017, Vienna, Austria

  Pejchal T., Musálek T., Kachtík L., Šikola T., Kolíbal M.: *MBE-grown Ge nanowires: The co-effect of atomic hydrogen and Au catalyst spreading.* Oral presentation (15 min).

- CEITEC PhD and Postdoc Retreat 2018
  26^{th} – 27^{th} April 2018, Telč, Czech Republic

  Pejchal T., Musálek T., Kachtík L., Šikola T., Kolíbal M.: *Bimetallic catalysts for MBE-grown Ge nanowires.* Poster presentation.

- Nanowire Week 2018
  11^{th} – 15^{th} June 2018, Hamilton, Canada

  Pejchal T., Kachtík L., Musálek T., Šikola T., Kolíbal M.: *Bimetallic catalysts for MBE-grown Ge nanowires.* Poster presentation.

- ICN+T 2018 – International Conference on Nanoscience + Technology
  22^{nd} – 27^{th} July 2018, Brno, Czech Republic

  Pejchal T., Kachtík L., Musálek T., Šikola T., Kolíbal M.: *Bimetallic catalysts for MBE-grown Ge nanowires.* Poster presentation.